gebiology

Geobiology (2014), **12**, 340–361 DOI: 10.1111/gbi.12088

3-D analysis of bacterial cell-(iron)mineral aggregates formed during Fe(II) oxidation by the nitrate-reducing *Acidovorax sp.* strain BoFeN1 using complementary microscopy tomography approaches

G. SCHMID,[1,†] F. ZEITVOGEL,[1,†] L. HAO,[1] P. INGINO,[1] M. FLOETENMEYER,[2] Y.-D. STIERHOF,[3] B. SCHROEPPEL,[4] C. J. BURKHARDT,[4] A. KAPPLER[1] AND M. OBST[1]

[1]*Center for Applied Geoscience, University of Tuebingen, Tuebingen, Germany*
[2]*Max Planck Institute for Developmental Biology, Tuebingen, Germany*
[3]*Center for Plant Molecular Biology, University of Tuebingen, Tuebingen, Germany*
[4]*NMI Natural and Medical Sciences Institute, University of Tuebingen, Reutlingen, Germany*

ABSTRACT

The formation of cell-(iron)mineral aggregates as a consequence of bacterial iron oxidation is an environmentally widespread process with a number of implications for processes such as sorption and coprecipitation of contaminants and nutrients. Whereas the overall appearance of such aggregates is easily accessible using 2-D microscopy techniques, the 3-D and internal structure remain obscure. In this study, we examined the 3-D structure of cell-(iron)mineral aggregates formed during Fe(II) oxidation by the nitrate-reducing *Acidovorax sp.* strain BoFeN1 using a combination of advanced 3-D microscopy techniques. We obtained 3-D structural and chemical information on different cellular encrustation patterns at high spatial resolution (4–200 nm, depending on the method): more specifically, (1) cells free of iron minerals, (2) periplasm filled with iron minerals, (3) spike- or platelet-shaped iron mineral structures, (4) bulky structures on the cell surface, (5) extracellular iron mineral shell structures, (6) cells with iron mineral filled cytoplasm, and (7) agglomerations of extracellular globular structures. In addition to structural information, chemical nanotomography suggests a dominant role of extracellular polymeric substances (EPS) in controlling the formation of cell-(iron)mineral aggregates. Furthermore, samples in their hydrated state showed cell-(iron)mineral aggregates in pristine conditions free of preparation (i.e., drying/dehydration) artifacts. All these results were obtained using 3-D microscopy techniques such as focused ion beam (FIB)/scanning electron microscopy (SEM) tomography, transmission electron microscopy (TEM) tomography, scanning transmission (soft) X-ray microscopy (STXM) tomography, and confocal laser scanning microscopy (CLSM). It turned out that, due to the various different contrast mechanisms of the individual approaches, and due to the required sample preparation steps, only the combination of these techniques was able to provide a comprehensive understanding of structure and composition of the various Fe-precipitates and their association with bacterial cells and EPS.

Received 31 October 2013; accepted 8 April 2014

Corresponding author: M. Obst. Tel.: +49 7071 2974701; fax: +49 7071 295059; e-mail: martin.obst@uni-tuebingen.de

INTRODUCTION

Iron is known to be an environmentally ubiquitous element and essential for all organisms. Iron can be redox-transformed in anoxic or suboxic zones whereby ferrous iron [Fe(II)] is oxidized by Fe(II)-oxidizing micro-organisms and subsequently ferric iron [Fe(III)] can be reduced by Fe(III)-reducing micro-organisms (Weber *et al.*, 2006; Konhauser *et al.*, 2011; Roden, 2012). In addition to direct metabolic Fe(II)-oxidation, it is suggested that Fe(II) can be oxidized by reactive by-products of bacterial metabolisms, for example, nitrite, which is an

[†]Both authors contributed equally to this work.

intermediate product of nitrate reduction and can lead to Fe(II) oxidation (Miot *et al.*, 2009a; Klueglein & Kappler, 2013; Klueglein *et al.*, 2014). A well-studied nitrate-reducing bacterium that induces Fe(II) oxidation is the *Acidovorax sp.* strain BoFeN1, isolated from an anoxic freshwater sediment (Kappler *et al.*, 2005). At circumneutral pH, Fe (III) is poorly soluble and induces cell encrustation in Fe (III)-precipitates and the formation of extracellular Fe(III)-precipitates in vicinity to the cells (Kappler *et al.*, 2005; Miot *et al.*, 2009b; Schaedler *et al.*, 2009). The microbial pathway of Fe(II) oxidation by nitrate-reducing, Fe(II)-oxidizing bacteria has been in the focus of several studies (Chakraborty *et al.*, 2011; Carlson *et al.*, 2012, 2013; Chakraborty & Picardal, 2013; Klueglein *et al.*, 2014). For BoFeN1, it was shown that Fe(II) is presumably oxidized indirectly by nitrite, which is an intermediate product of nitrate reduction, rather than by direct enzymatic Fe(II) oxidation (Miot *et al.*, 2009a; Klueglein & Kappler, 2013; Klueglein *et al.*, 2014). However, based on the current knowledge, an enzymatic contribution to Fe(II) oxidation cannot be ruled out completely. Initial iron phases formed by BoFeN1 were mainly a mixture of green rust (a mixed Fe(II)/Fe(III)-hydroxide), a poorly crystalline Fe(III)-hydroxide, and goethite when cultivated with Fe(II) (Pantke *et al.*, 2012). After complete Fe(II) oxidation, most studies identified goethite as the final Fe(III) mineral phase (Kappler *et al.*, 2005; Hohmann *et al.*, 2010). In previous studies, BoFeN1 revealed different precipitation patterns resulting from precipitation of Fe(III) such as layers of iron minerals in the periplasm, structures of different shapes attached to the cell surface, minerals within the cytoplasm, extracellular structures enclosing the cells (shells), and filamentous structures in vicinity to cells (Kappler *et al.*, 2005; Miot *et al.*, 2009a,b, 2011; Schaedler *et al.*, 2009; Klueglein *et al.*, 2014). The knowledge we have so far on structures formed by BoFeN1 is based on a great number of different techniques, such as scanning electron microscopy (SEM) (Kappler *et al.*, 2005; Schaedler *et al.*, 2009), scanning transmission (soft) X-ray microscopy (STXM) (Miot *et al.*, 2009a,b; Hitchcock *et al.*, 2012; Pantke *et al.*, 2012), transmission electron microscopy (TEM) (at whole cells as well as ultrathin sections) (Miot *et al.*, 2009b), confocal laser scanning microscopy (CLSM) (Klueglein *et al.*, 2014), cryo-TEM and cryo-electron microscopy of vitreous sections (CEMOVIS) (Miot *et al.*, 2011). Tilt series of a BoFeN1 cell were previously recorded by Miot *et al.* (2009b), but no 3-D reconstruction was performed. Despite these thorough and careful studies, the present knowledge on the structures formed by BoFeN1 remains incomplete. The techniques that have so far been applied only provide 2-D surface images (e.g., SEM) or projections of cells (e.g., STXM) or isolated sections through a volume (TEM with ultrathin sections). With respect to 3-D structure, this information is either incomplete or ambiguous. For example, in projections and surface images, it is not possible to clearly distinguish intracellular and extracellular structures. 2-D projections of 3-D volumes could lead to misinterpretation of structures, for example, based on 2-D images of iron encrusted BoFeN1 cells, it could be assumed that the cytoplasm as the periplasm is filled with iron minerals. Also, in 2-D, a clear distinction between extracellular mineral shell structures and cells enclosed in these can be ambiguous. Ultrathin sections can tackle this problem, but do not provide information on entire cells. In addition, most analyses focused on isolated cells and did not show the arrangement of cells within cell-(iron)mineral aggregates. The goal of this study was to use a combination of established and novel 3-D microscopy approaches to identify and to distinguish between patterns of biogenic iron mineral precipitation. This allows us to visualize the entire volume of encrusted BoFeN1 cells and to reveal and distinguish between different precipitations patterns. In addition, binding sites for iron, as, for example, organic carbon in the periplasm (Miot *et al.*, 2009b, 2011) can be proven using BoFeN1 samples prepared in a hydrated state for STXM tomography; that allows us to obtaining chemical maps with 3-D structural information of the whole cell volume.

For several reasons, it is important to close these knowledge gaps. First, structural information in general can help to elucidate the mechanisms that lead to their formation. Second, and more specifically, different cell-(iron)mineral structures formed by BoFeN1 have shown a different behavior toward their environment. For example, different types of extracellular and intracellular iron precipitates were shown to differ significantly regarding their sorption properties for As-species (Hitchcock *et al.*, 2012). As a basis for further research, it is therefore important to know the different cell-(iron)mineral structures that can possibly form, and to be able to analyze the samples in a way that allows to distinguish between these structures.

Therefore, we selected a number of different 3-D approaches that provide highly complementary information on both the 3-D structure and chemical composition of the cell-(iron)mineral aggregates formed by the strain BoFeN1. Spatially highly resolved tomography approaches provide detailed insights to understand the spatial arrangement and associations between the BoFeN1 cells (including cytoplasm and periplasm), their extracellular polymeric substances (EPS), and the different forms and stages of biogenic Fe-mineral products, and thus reveal information which is non-accessible in surface or projection images as produced by conventional 2-D imaging techniques. All these microscopy tomography techniques are technically sophisticated and have become more commonly available in the last decades allowing high-resolution 3-D imaging. As many of the approaches used here are relatively new in bio-, geo-, and environmental science, this study will also

discuss the advantages and limitations of different microscopy tomography approaches. Our approach included electron microscopy techniques such as focused ion beam (FIB)/SEM tomography (Holzer *et al.*, 2004) and TEM tomography (Midgley & Weyland, 2003; Frank, 2006) to study cell-(iron)mineral aggregates formed by BoFeN1. Complementary to the electron microscopy tomography approaches, synchrotron-based STXM tomography was applied, which combines soft X-ray spectroscopy (XAS) with high-resolution tomography and thus results in quantitative 3-D distribution measurements of elements or chemical species (Johansson *et al.*, 2007; Hitchcock *et al.*, 2008; Obst *et al.*, 2009; Wang *et al.*, 2011; Schmid *et al.*, 2014). Finally, CLSM was used to upscale the analysis to larger cell-(iron)mineral aggregates; this technique also allows to obtain chemical information of in vivo, fully hydrated samples by detecting fluorescence and reflection signals, albeit at a lower spatial resolution than offered by the other techniques applied (Kuehn *et al.*, 1998; Lawrence *et al.*, 2003; Neu *et al.*, 2010). Table 1 provides an overview of the basics, advantages, and limitations of the different tomography approaches. The microscopy tomography techniques applied in this study are described in detail in the supporting information.

Important considerations when analyzing biological samples such as cell-(iron)mineral aggregates produced by strain BoFeN1 are artifacts that can arise during sample preparation for the different tomography methods. Cell-(iron)mineral aggregates were either air-dried for TEM and STXM tomography, cryo-fixed, freeze-substituted, and embedded in epoxy resin for FIB/SEM, or stained with fluorescent dyes in hydrated state for CLSM. Preparation methods have a strong influence on the preservation of the sample. Distortions of the structure of biological samples can be induced by virtually any preparation method. Compromises often have to be made between structural preservation and preservation of the chemical composition. The most obvious artifacts are expected for air-drying, where surface tensions can lead to agglomeration and shrinkage. For the present type of sample, the most delicate part is the matrix of EPS that is even susceptible to collapse during dehydration with solvents, which is a necessary step for both critical point drying (CPD) and resin embedding (Dohnalkova *et al.*, 2011). In order to prevent or to identify and to minimize artifacts during sample preparation, we also used a novel approach for STXM tomography to analyze spectromicroscopic BoFeN1 samples in hydrated state (Schmid *et al.*, 2014).

To summarize, the main objectives of this study are twofold. First, we intend to study in 3-D the structure, chemical composition, and spatial arrangement of the different precipitates encrusting the cells of the nitrate-reducing *Acidovorax sp.* strain BoFeN1 and to investigate the influence of EPS on the formation of biogenic minerals and cell-(iron)mineral aggregates by combining information from four complementary 3-D microscopy techniques. Second, our goal is to investigate the specific advantages and limitations of the methods applied with respect to their sample preparation and accessible information.

MATERIALS AND METHODS

Microbial growth and growth conditions

The chemoorganotrophic, nitrate-reducing ß-proteobacterium *Acidovorax sp.* strain BoFeN1 was used as a model bacterium that induces Fe(II) oxidation. Strain BoFeN1 was described to grow mixotrophically by oxidizing ferrous iron and acetate as organic cosubstrate (Kappler *et al.*, 2005; Muehe *et al.*, 2009). BoFeN1 was cultivated in anoxically prepared 22 mM bicarbonate-buffered mineral medium supplemented with 10 mM Na nitrate and 5 mM Na acetate (Hegler *et al.*, 2008). Reduced phosphate concentrations of 1 mM instead of initial 4.4 mM were used in the medium to reduce precipitation of a whitish, poorly crystalline Fe(II) phosphate after addition of 10 mM Fe(II) Cl_2 (Hohmann *et al.*, 2010). After 48 h, the medium was filtered with a 0.22-µm sterile filter (mixed cellulose esters, Fisherbrand, Loughborough, England) in an anoxic chamber (GS Glovebox Systemtechnik, Malsch, Germany) under 100% N_2 atmosphere to obtain an Fe(II)-precipitate-free medium with Fe^{2+} concentrations of 8–10 mM and photometrically measured (Vogler, 1966) phosphate concentrations of 15–20 µM. BoFeN1 was cultivated anoxically either in 58-mL serum bottles or in 15-mL culture tubes with N_2/CO_2 (90/10, v/v)-flushed headspace. Serum bottles and tubes were closed with butyl stoppers. Afterward, filtered medium was supplemented with anoxic 10 mM Na nitrate and 5 mM Na acetate, and 5% inoculum was added from a fresh acetate/nitrate grown BoFeN1 stock culture. BoFeN1 cultures were incubated in the dark at 28 °C. Fe(II) oxidation after BoFeN1 inoculation to the medium is observed already within 30 min, and Fe(II) oxidation is completed after 4–6 days (Kappler *et al.*, 2005; Miot *et al.*, 2009b; Muehe *et al.*, 2009; Klueglein & Kappler, 2013). BoFeN1 cultures were grown for at least 6 days to ensure complete Fe(II) oxidation, and formed cell-(iron)mineral aggregates were analyzed by FIB/SEM, STXM, and CLSM. Additionally, 1-day-old BoFeN1 cultures were analyzed with STXM tomography and TEM tomography to study an early stage of Fe(II) oxidation.

Sample preparation for FIB/SEM tomography

Aliquots of samples were taken under oxic conditions from BoFeN1 cultures after complete Fe(II) oxidation (6 days), centrifuged, and taken up with 200-µm cellulose capillaries for easier handling. The capillaries were cut into segments of approximately 2 mm length that fit precisely into the

Table 1 Comparison of the different tomography techniques regarding their information content, technical aspects, advantages, and limitations as applied in this study. For calculation of the resolution in angle-scan methods, see supporting information

Acquisition technique	Contrast generation	Spatial resolution (in x,y,z direction) [nm^3]	Typical sample thickness	Sample preparation	Sample damage	Advantages	Potential limitations
FIB/SEM tomography	Electron density	~4 × 4 × 4	10–100 μm	Embedding in epoxy resin (preceded by fixation and dehydration) Staining	The analyzed volume is removed by serial ion milling	Large sample area Analyzed sample area can be part of larger samples Wide-spread commercial machines available No numerical reconstruction Automatic data acquisition	No chemical information* Difficult selection of sample area Destruction of sample Low data acquisition rate
TEM tomography	Electron density	~2 × 13 × 20†	≤100 nm†	Staining Ultrathin sections (fixation, dehydration, embedding) Whole cells (freeze-, air-drying or CPD)	Beam damage	High resolution Wide-spread commercial machines available Fast automatic data acquisition	No chemical information (except TEM-ESI)† Missing wedge (single axis)† Reconstruction artifacts Limited sample thickness†
STXM tomography	X-ray absorption edges (NEXAFS)	~40 × 40 × 50	≤300 nm at C-1s Absorption edge	Air-drying Wet preparation	Beam damage	Elemental analysis (organic and inorganic components) Chemical information (redox state, mineral phase) Hydrated samples Quantitative information	Tricky sample preparation (wet-cell tomography) Low data acquisition rate (manual operation needed) Absorption saturation Missing wedge Limited synchrotron time
CLSM	Fluorescence Reflection	~200 × 200 × 200	50–150 μm	Staining with dyes Wet preparation		Chemical labeling Wide-spread commercial machines available and easy aces No numerical reconstruction Fast automatic and easy data acquisition	Cross-correlation of dyes Lower spatial resolution Bleaching Drift of the sample

CLSM, confocal laser scanning microscopy; CPD, critical point drying; FIB/SEM, focused ion beam/scanning electron microscopy; STXM, scanning transmission (soft) X-ray microscopy; TEM, transmission electron microscopy.

*In combination with energy dispersive X-ray (EDX) spectroscopy, it is possible to get chemical information at lower spatial resolution (Lasagni *et al.*, 2008).

†These are typical values for single-axis TEM tomography with 120 kV. Other setups allow for reducing missing-wedge artifacts by dual-axis tomography (Mastronarde, 1997), higher resolution (Midgley & Weyland, 2003), and larger samples thickness up to 500 nm (Biskupek *et al.*, 2010) using scanning transmission electron microscopy (STEM) with up to 300 kV acceleration voltage, and even chemical information using TEM in combination with energy-selective imaging (ESI) (Weyland & Midgley, 2003; Messaoudi *et al.*, 2013).

150 μm cavity of an aluminum platelet for high-pressure freezing, filled with 1-hexadecene. The platelets were sandwiched with a second platelet without cavity, high-pressure frozen using a HPM 010 (Bal-Tec, Balzers, Liechtenstein), and freeze-substituted in 1.25% glutaraldehyde in acetone using a Leica freeze substitution unit (Leica Microsystems, Wetzlar, Germany). The temperature was increased stepwise, the sample was first kept at −90 °C for 40 h, raised to −60 °C over 6 h and kept at −60 °C for 4 h, raised to −40 °C over 4 h, raised to 0 °C over 2 h, and kept at 0 °C for 1 h. Samples were then washed five times in acetone and infiltrated with Epon (10% Epon resin in acetone for 2 h, 25% Epon overnight, 50% Epon for 8 h, 75% Epon overnight, 100% Epon for 8 h, 100% Epon for 20 h, then placed in embedding molds containing fresh Epon resin) and polymerized for 2 days at 60 °C.

Heavy metal stains (such as osmium tetroxide, lead citrate, or uranyl acetate for contrasting biological samples for TEM) were not used as preliminary experiments had shown that Fe-accumulations would reliably highlight the structures of interest such as encrusted cells and Fe-minerals. In turn, the contrast observed in electron microscopy is mainly caused by the biogenic Fe-minerals, and Fe(III) complexed and sorbed to the biological structures. The surface of the resulting epoxy block was prepared on an ultramicrotome (Om U3, C. Reichert, Austria) using a glass knife followed by a diamond knife (DuPont, Wilmington, DE, USA). The block with embedded cell-(iron)mineral sample was mounted on an SEM sample holder (Plano, Wetzlar, Germany, model G301S) and coated with AuPd using a Balzers Union SCD 040 sputter coater (Bal-tec, Liechtenstein).

Sample preparation for TEM tomography

Aliquots of cell-(iron)mineral aggregates of an early Fe(II) oxidation state (after 1 day of incubation) were prepared in the anoxic chamber similar as described in detail in the next section for air-dried STXM tomography samples on a Formvar-coated 300 mesh Cu TEM grid (Plano, Wetzlar, Germany). Due to the thickness of approximately 1 μm (i.e., the whole structure, which is not solid) of these types of samples, embedding of the samples was not appropriate. As we were interested mostly in the distribution of the minerals within the small aggregate, air-drying turned out to be a good compromise, although the ultrastructure of the cell is not preserved by this approach. As our samples are significantly thicker in structure as compared to typical TEM samples such as ultrathin sections, significantly better resolved reconstructions can in principle be achieved for the latter.

Sample preparation for STXM tomography

For STXM tomography, two types of sample preparation methods were applied. For one preparation method, cell-(iron)mineral aggregates were prepared by air-drying the sample on 300 mesh TEM grids from which a stripe was cut as described by Obst *et al.* (2009). For the other preparation method, liquid cell-(iron)mineral suspension was injected into Luxel wet cells (Schmid & Obst, 2014; Schmid *et al.*, 2014). For preparation of the air-dried sample on 300 mesh Cu TEM grids, aliquots of 0.5–1 mL of BoFeN1 cell-(iron)mineral suspension were sampled anoxically with a syringe at an early Fe(II) oxidation stage (after 1 day) and after complete Fe(II) oxidation (after 7 days). In the anoxic chamber, aliquots were centrifuged and resuspended in sterile deionized water to remove remaining Fe^{2+} and salts from the medium. A few droplets of the washed cell-(iron)mineral suspension were placed on a Formvar-coated 300 mesh Cu TEM grid, blotted with filter paper, and air-dried in the anoxic chamber. Appropriate spots, that is, spots with isolated cell-(iron)mineral aggregates, ideally oriented parallel to the rotation axis were selected for STXM tomography under an optical microscope. The grid was cut into stripes, which were aligned onto brass rods (Ø of 0.8 mm) as described by Schmid and Obst (2014).

Cell-(iron)mineral aggregates for analyzing hydrated samples were prepared differently as described in detail by Schmid *et al.* (2014). In brief, about 1.5 mL of a sample taken from a BoFeN1 culture after complete Fe(II) oxidation (after 7 days) was centrifuged and resuspended in medium free of acetate, nitrate, and Fe^{2+} to keep the cells alive but inactive for the transport to the synchrotron. Cell-(iron)mineral suspension was injected into a Luxel wet cell (Luxel, Friday Harbor, WA, USA) on site of the soft X-ray spectromicroscopy (SM) 10ID-1 beamline at the Canadian Light Source (CLS, Saskatoon, Canada) immediately prior to the STXM tomography measurements to prevent dehydration of the sample. To this end, a few μL aliquot of the cell-(iron)mineral suspensions was taken up with a glass micropipette (tip Ø of 2–5 μm) attached to a self-made portable microinjection system. Using a glass micropipette, it was possible to carefully inject droplets of the suspended sample into the interspace between two polyimide LUXFilm® membranes of a Luxel wet cell. The hole punched with the micropipette was subsequently sealed with nail polish.

Sample preparation for CLSM

Around 200 μL cell-(iron)mineral suspension of BoFeN1 culture was sampled for CLSM after 15 days [no remaining Fe(II)]. Fluorescent probes were then added sequentially, and the samples were incubated for 1 h, unless otherwise mentioned at 37 °C in the dark to prevent photo-bleaching effects. In contrast to the previously described methods, no centrifugation or washing steps were applied to preserve the pristine conditions of the

cell-(iron)mineral aggregates. To label DNA, SYTO® 9 Green Fluorescent Nucleic Acid Stain (Molecular Probes, Carlsbad, CA, USA) was added to the sample reaching a final concentration of 1.22 μM. A fluorescent Fe^{3+}-probe (Zhang *et al.*, 2011) was added to the sample to a final concentration of ~70 μM followed by 2-h incubation. To label polysaccharides in the EPS, Wheat Germ Agglutinin (WGA) Alexa Fluor® 633 conjugate (Molecular Probes) was added to a final concentration of 8.58 μg mL^{-1}. WGA binds to a variety of polysaccharides such as chitin, N-acetyl neuraminic acid, glycoproteins, fetuin, or chitobiose (Lawrence *et al.*, 2007). Finally, 2 μL of the stained sample was applied on a glass slide to which a cover slip was attached using a 120-μm-thick spacer (SecureSeal™, Grace Biolabs, Bend, OR, USA) and sealed with nail polish. All preparation steps were conducted under anoxic conditions in an anoxic chamber, except the incubation of the anoxically sealed sample at 37 °C.

Analytical methods

FIB/SEM tomography

Focused ion beam/scanning electron microscopy (FIB/SEM) tomography data were acquired using a Zeiss Auriga CrossBeam instrument at the Natural and Medical Sciences Institute at the University of Tuebingen (NMI; Reutlingen, Germany). The sample was tilted to 54°, and the surface moved into the coincidence point of ion and electron beam at a working distance of 5 mm. Preliminary experiments had shown that for this particular type of sample, the ultramicrotome-prepared surface was sufficiently smooth to omit electron beam or ion-beam-induced deposition (EBID/IBID) of a protective layer of Pt or other materials that is frequently suggested (Knott *et al.*, 2011). An initial blockface was prepared using a FIB current of 10 nA at an acceleration voltage of 30 kV. For serial sectioning, a FIB current of 2 nA was applied. Images of 2048 × 1536 pixels were acquired using an energy-selective backscatter (EsB) electron detector at an acceleration voltage of 1.8 kV, a detector grid tension of 1.5 kV, dwell time of 25.6 μs, and a pixel size of 9.9 × 9.9 nm^2. The nominal slice thickness was 10 nm, accounting for approximately isotropic voxels. These settings would allow us to render 3-D images at a resolution which is sufficient to distinguish the features of interest, but in principle well outreached by state-of-the-art low-voltage field-emission (FE) SEM. The final dataset consisted of 556 slices, corresponding to a volume of (nominally) 20.3 × 15.2 × 5.6 $μm^3$. Data processing was carried out using Fiji (Schindelin *et al.*, 2012). A custom-made plug-in for Fiji was used to pre-align the slices according to the bright upper edge and to cut off this edge. Subsequently, slices were automatically aligned using the StackReg plug-in (Thévenaz *et al.*, 1998) in translation mode (correcting only for shift in *x*- and *y*-direction). Structures that were not connected to the main cell-(iron)mineral aggregate (see FIB/SEM results) were deleted using the 'fill selection' function in the 3D Viewer plug-in (Schmid *et al.*, 2010). In the same way, typical cells representing different encrustation patterns were isolated from the main dataset for detailed rendering. UCSF Chimera (Pettersen *et al.*, 2004) was used for 3-D rendering. Prior to rendering, a histogram threshold was applied, but no segmentation. In the reconstructed volume, cells were counted and classified according to the above-mentioned encrustation patterns. Partial cells at the edges of the reconstructed volume could be classified unambiguously and thus were included in the count.

TEM tomography

Transmission electron microscopy tomography data were acquired with a FEI™ Tecnai G^2 Spirit Bio TWIN (FEI Company, Hillsboro, OR, USA) operated at 120 kV at Max Planck Institute for Developmental Biology Tuebingen (MPI; Tuebingen, Germany). Using the SERIALEM software (Mastronarde, 2005), a tilt series of 121 projection images was acquired with a Gatan UltraScan™ (Gatan Inc., Pleasanton, CA, USA) camera over a tilt range of ±60° with an angle step size of 1°. TEM autofocus was applied for every 6th image while within the range of ±45° and for each image while outside this range due to stronger focus change. Images consisted of 4098 × 4098 pixels with a pixel size of 0.98 × 0.98 nm^2. Prior to reconstruction, images were downscaled by a factor of 2 using bilinear interpolation and converted to 8-bit grayscale format in Fiji. Image alignment and 3-D reconstruction was performed using the IMOD package (Kremer *et al.*, 1996). The TEM tomography dataset was reconstructed using the simultaneous iterative reconstruction technique (SIRT) with 200 iterations with a radial filter cutoff of 0.4 and a falloff of 0.05 (Gilbert, 1972). For representation, images were inverted to make electron-dense structures appear bright. Images were rendered using Chimera (Pettersen *et al.*, 2004). The dataset was downscaled by a factor of 2 for an overview image, and a mask was created using ilastik (Sommer *et al.*, 2011) in batch mode and superimposed on the reconstruction to cover streaking artifacts introduced during the SIRT procedure. For detailed images, subvolumes of the unaltered reconstruction were used. Histogram thresholding was applied in all cases to separate the cell-(iron) mineral aggregate from background noise.

STXM tomography

Scanning transmission (soft) X-ray microscopy tomography measurements were performed at the SM 10ID-1 beamline of the CLS in Saskatoon (Kaznatcheev *et al.*, 2007). Images were recorded from different angles at selected X-ray energies that are specific for X-ray absorption of organic carbon (e.g., proteins, lipids, and polysaccharides)

and Fe-minerals (Schmid & Obst, 2014; Schmid *et al.*, 2014). Therefore, a custom-made tomography sample holder based on a stepper motor and gearbox (ADM0620, 061K1024:1, Faulhaber, Schoenaich, Germany) was used to rotate the sample over a typical angle range of ±72° at 4° steps. Energies for C K-edge (C-1s) and O K-edge (O-1s) were calibrated by measuring the 3p Rydberg peak of gaseous CO_2 and for Fe L_3-edge (Fe-2p) using the dominant peak of Fe(III) at 708.7 eV (Miot *et al.*, 2009b). The images were converted from transmission scale into linear absorbance scale (denoted as optical density, OD): $OD = -\ln(I/I_0)$; wherein I denotes the measured photon intensity for a pixel of the sample and I_0 the transmitted photon intensity in an empty spot adjacent to the sample. Due to limited synchrotron time and to limit beam-induced damage, for tomography experiments only images at selected, specific X-ray absorption energies were acquired (denoted as stack map), instead of acquiring a full spectrum (denoted as stack) at every rotation angle. Quantitative chemical component maps were calculated from the acquired stack maps using the AXIS2000 software (Hitchcock, 2013) either by singular value decomposition (SVD) (Koprinarov *et al.*, 2002) for measurements at the O-1s edge or by subtracting an image in the pre-edge energy region from an image at a characteristic X-ray absorption energy for measurements at the C1-s and Fe-2p edges (Schmid & Obst, 2014). This was necessary as several selected energies of the stack maps at the C-1s and Fe-2p edges were absorption-saturated with respect to their OD (OD > ~2) (Dynes *et al.*, 2006; Hanhan *et al.*, 2009; Bourdelle *et al.*, 2013) because of sample thickness, so that SVD could not be applied. Selected energies at the C-1s edge were 280 eV for the pre-edge (no C-1s specific X-ray absorption) and at 288.2 eV for the dominant protein peak (C-1s→$\pi^*_{C=O}$ transition) with minor contributions of other organic species such as of polysaccharides and lipids (Lawrence *et al.*, 2003), and these chemical maps were referred to as organic carbon maps. At the Fe-2p edge, images were acquired at 705.1 eV for the pre-edge and at 723.8 eV as X-ray absorption peak for iron minerals at the Fe L_2 edge (Bourdelle *et al.*, 2013) that is sufficiently low in OD to prevent absorption saturation even for thicker samples. No problems with absorption saturation were encountered at the O-1s edge (OD < 2) allowing to apply spectral fitting by SVD. Therefore, selected energies for spectral fitting at the O1s edge were 528, 530, 532.2, and 538 eV for both air-dried samples and 528, 532.2, and 538 eV for the hydrated sample. The X-ray absorption peak at 532.2 eV is a dominant protein peak (O1s→$\pi^*_{C=O}$ transition) (Stewart-Ornstein *et al.*, 2007) with minor contributions of other organic species such as polysaccharides, and these chemical maps are referred to as protein maps.

Pixel spacings of 20 × 20 nm^2 and 25 × 25 nm^2 were selected for the completely oxidized sample and for both the hydrated and the dry sample at an early stage of Fe(II) oxidation, respectively. Quantitative maps from the O-1s edge (OD < 2) were derived from fitting with normalized spectra of reference compounds of albumin (Fig. S1) (Stewart-Ornstein *et al.*, 2007), an biogenic Fe-precipitate spectrum representing a Fe(III)-(oxyhydr)oxide phase containing minor contributions of organic carbon material (e.g., EPS) (Fig. S1), and a calculated, non-specific background spectrum based on the atomic scattering factors (Henke *et al.*, 1993). The biogenic Fe-precipitate spectrum was extracted from a region with extracellular mineral aggregates of the early Fe(II) oxidation stage sample at the O-1s absorption edge and was very similar to the spectrum of ferrihydrite. O-1s measurements of the hydrated sample (OD < 1.7) were also fitted using spectra of protein, ferrihydrite, water (Fig. S2), and the above-mentioned non-specific background spectrum accounting for all components absorbing below the O-1s edge (Schmid *et al.*, 2014). Lower residuals for the fits, however, were obtained using a reference spectrum of ferrihydrite instead of goethite. For practical reasons, the I_0 signal was measured within the wet-cell area close to the sample, which led to the effect that a significant part of the water signal was removed during conversion to OD. To correct for this, the pixel gray values were raised by a constant corresponding to 120 nm in the 2-D projections of the water component. See also Schmid *et al.* (2014) for a detailed description of the analyzed wet-cell sample.

Quantitative maps that represent a projection of the distribution of the respective chemical species were calculated for each tilt step. The resulting datasets were reconstructed with IMOD applying SIRT with 400 iterations, a radial filter cutoff of 0.4 and a falloff of 0.05. 3-D stack maps were aligned with respect to each other using a custom-made plug-in for Fiji. The 'subtract background' function of Fiji was applied, which is based on a rolling-ball algorithm (Sternberg, 1983), to remove background noise in the 3-D component maps. Due to the particularly high background in the C-1s datasets, a binary mask was created with ilastik (Sommer *et al.*, 2011) to remove background signal in the empty areas adjacent to the cell-(iron)mineral aggregates. This background was likely caused by the Formvar-film supporting the sample. 3-D rendering was performed with UCSF Chimera (Pettersen *et al.*, 2004). Histogram thresholding was applied for all 3-D stack maps.

For quantitative calculations of the chemical component masses within the analyzed volumes, the lower end of the histogram of the 3-D component maps was clipped at the background intensity value. The background intensity was determined as the mean gray value of a representative empty area in an average projection of the stack along the z-axis.

Confocal laser scanning microscopy

Image stacks of the stained BoFeN1 samples were acquired with an upright Leica TCS SPE system (Leica Microsystems,

Wetzlar, Germany) equipped with four lasers (405, 488, 561, and 635 nm) using a water immersion objective (ACS APO 63.0×, NA = 1.15). Datasets were obtained in sequential mode with an image size of 512 × 512 pixels. Blind deconvolution in 10 iterations using the Auto-Quant™ Deconvolution (integrated in LAS-AF, Leica Microsystems, Wetzlar, Germany) algorithm of the LEICA LAS AF software suite was applied to image stacks. For 3-D reconstruction, isotropic voxels were obtained by reslicing the deconvolved image stacks using Fiji. 3-D rendering of the dataset was carried out with UCSF Chimera. More information about the CLSM settings is provided in the supporting information.

RESULTS

In the following paragraph, we present our major findings regarding the structure and formation of cell-(iron)mineral aggregates formed during Fe(II) oxidation by the nitrate-reducing *Acidovorax sp.* strain BoFeN1 obtained with the individual microscopy tomography approaches. In the discussion section, we then integrate all results into an overall interpretation of the different encrustation patterns.

FIB/SEM tomography

We focused on the analysis of an area containing an agglomeration of bacterial cells and Fe-precipitates, which were cryo-fixed, freeze-substituted, and embedded. It turned out that most cells and iron minerals within that volume formed one interconnected structure (Figs 2 and S3). While in the present dataset it is not possible to distinguish sorbed iron from Fe-minerals, TEM images published by Klueglein *et al.* (2014), which were taken from the same batch of samples, show that most of the contrast is generated by crystalline phases. A movie (movie S3) showing the whole cell-(iron)mineral aggregate can be downloaded in the supporting information. Previously applied methods were not able to access the internal structure of cell-(iron)mineral aggregates.

Identification of cellular encrustation patterns

At the chosen voxel dimensions, it was possible to identify in detail different cellular 'encrustation patterns' (i.e., spatial patterns formed by intimately associated cells and iron minerals) that will be briefly described in the following. Our data provide conclusive 3-D models for those structures. This extends previous knowledge by providing both a reconstruction of the outside appearance and a detailed model of the interior. (i) Some cells did not show any significant iron accumulations. As they did not produce much contrast, these non-encrusted/iron-free cells were barely visible in blockface images and could not be rendered in 3-D. Blockface images of non-encrusted cells are shown in Figure 2B,C. (ii) The most frequently observed type of microbial precipitation pattern showed an Fe-rich layer within the periplasmic space of the cell (Fig. 1A, Fig. 2H). This could co-occur with other types of mineralization, for example, extracellular precipitates or minerals in the cytoplasmic space. (iii) A large number of cells were covered in an epicellular layer of spike- or platelet-shaped iron minerals (Fig. 1B, Fig. 2D). (iv) As a second type of epicellular encrustation, we observed bulky structures of apparently undefined shape attached to the cell surface (Fig. 1C, Fig. 2I). (v) Some cells were surrounded by an extracellular

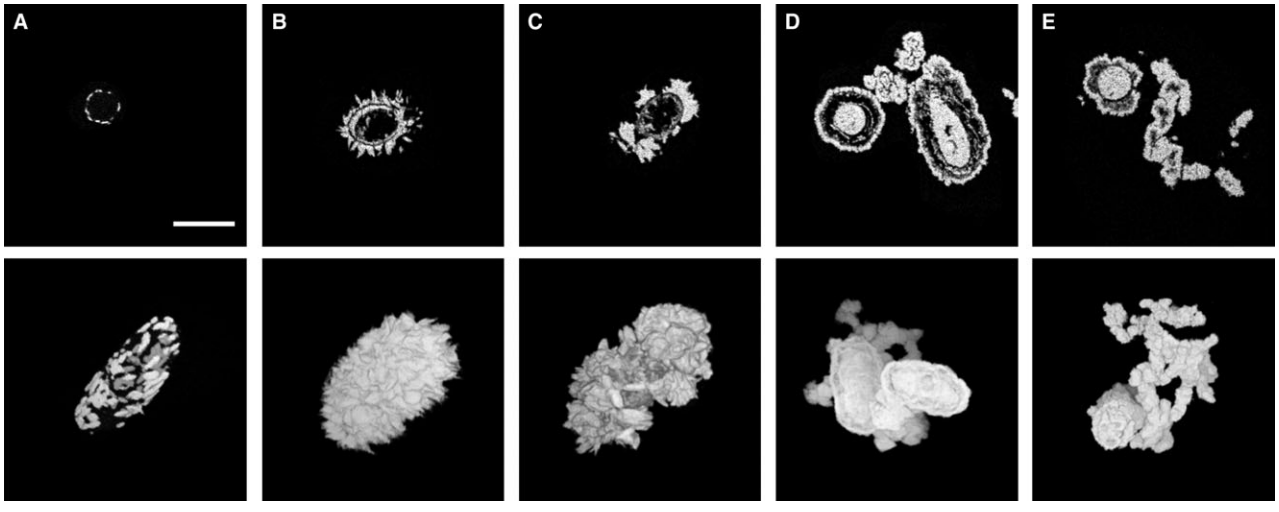

Fig. 1 Different encrustation patterns of BoFeN1 as observed by focused ion beam/scanning electron microscopy (FIB/SEM) tomography and described in Table 2. The upper row shows individual blockface images, the lower row shows the respective 3-D reconstructions carried out using Chimera. 3-D reconstructions are not to scale. Scale bar (1 μm) only applies to upper row.

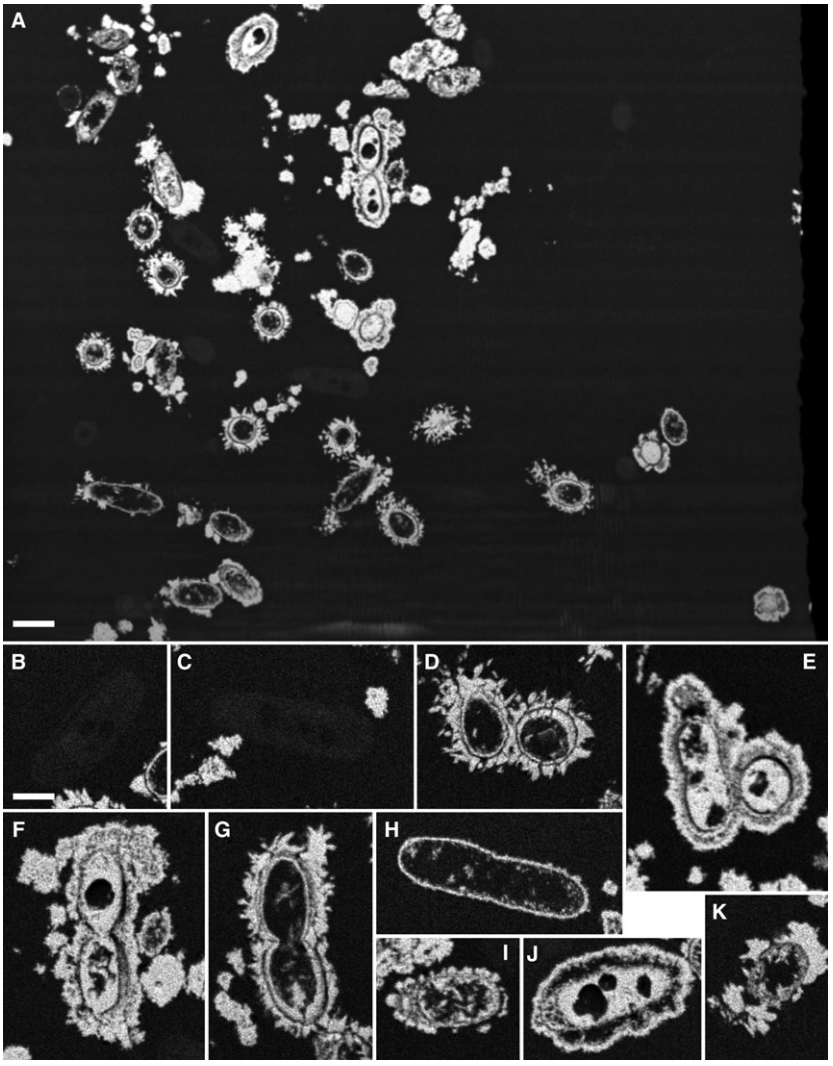

Fig. 2 Selected views from focused ion beam/scanning electron microscopy (FIB/SEM) volume: (A) tilted view showing spatial clustering of encrustation patterns within the cell-(iron)mineral aggregates; (B) blockface image of non-mineralized cell; (C) blockface image of non-mineralized cell attached to extracellular 'chain' structures; (D) blockface image intergrown spiky minerals of two cells; (E) tilted view of extracellular 'shells' enclosing two cells; (F–H) blockface images of dividing cells; (I,J) blockface images of cells with bulging cell poles; (K) blockface image of cell with minerals attached to inner membrane [scale bars 1 μm (A)/500 nm (B to K)].

mineralized layer that was not connected to the cell surface and formed a shell enclosing single or multiple cells (Fig. 1D, Fig. 2J). Mineralized structures enclosing cells are known from bacteria that form cylindrical sheeths (Konhauser, 2007). The present structures, however, were far from cylindrical and rather resembled large cells. (vi) Such mineral shells seemed to co-occur with intracellular iron mineral accumulations that filled a considerable part of the periplasmic space (Fig. 2E). (vii) In addition to cell-associated Fe-precipitates, we observed extracellular Fe-precipitates that consisted of interconnected, chain-like agglomerations of globular structures (Fig. 1D,E, Fig. 2F). These chains were much longer than previously known (Miot *et al.*, 2009b). In fact, some parts of the cell-(iron) mineral aggregate had a network-like appearance due to the presence of those chains (see movie S3). As confirmed also by previous STXM measurements (data not published), such structures often had a non-mineralized interior and seemed to extend from extracellular iron mineral shells or were otherwise connected to cells. These findings confirm and extend prior knowledge by providing 3-D information on structures so far only known from surface or 2-D projection images. Table 2 summarizes the different described cellular mineralization patterns as observed in the FIB/SEM results.

Abundance of encrustation types

Due to the large number of cells within the analyzed volume, a number of observations could be made on the cell level. In total, 165 cells could be distinguished within the reconstructed volume (Figs 2 and S3). Thereof, 46 cells (i.e., 28%) were of the non-mineralized type. A total of 33 cells (20%) had spiky precipitates, 52 cells (32%) bulky precipitates on the cell surface. A total of 31 cells (19%) were enclosed by extracellular shells. Some cells could not be unambiguously classified as they probably represented intermediate stages, and some cells were classified to

Table 2 Overview of the different encrustation patterns found for BoFeN1 when cultivated with Fe(II) and analyzed with FIB/SEM, TEM, STXM, and CLSM

	Encrustation patterns	Encrustation description	Indications and first descriptions
(1)	Mineral-free	No iron mineral accumulations	Observed by SEM (Kappler *et al.*, 2005)
(2)	Periplasm	Periplasm filled with iron minerals	Observed by scanning transmission electron microscopy (STEM) and STXM (Miot *et al.*, 2009b) Shown in Figs 1A and 2H
(3)	Spikes	Spike- or platelet-shaped iron minerals on cell surface	Observed by SEM (Kappler *et al.*, 2005) Platelet form revealed by TEM tomography Shown in Figs 1B and 2D
(4)	Bulky	Bulky structures of no particular shape on cell surface	Could be artifact of collapsed cell-mineral aggregates Shown in Figs 1C and 2I
(5)	Shells	Extracellular mineral shells enclosing one or multiple cells; separated from cell surface	Sometimes partly connected to cell surface Both shells and bulky structures might account for globular structures on cell surface as frequently observed by STEM and TEM (Miot *et al.*, 2009b) Seems to co-occur with mineralized cytoplasm Shown in Figs 1D and 2F
(6)	Cytoplasm mineralization	Cytoplasm filled with iron minerals	Seems to co-occur with shells Observed by STXM (Hitchcock *et al.*, 2012)
(7)	Extracellular globules	Chain-like agglomerations of globular structures	Described as 'filaments' by TEM and STEM (Miot *et al.*, 2009b) Might be extensions of shells Globules can be hollow and associated with organic molecules Shown in Figs 1E and 2F

CLSM, confocal laser scanning microscopy; FIB/SEM, focused ion beam/scanning electron microscopy; STXM, scanning transmission (soft) X-ray microscopy; TEM, transmission electron microscopy.

correspond to more than one of the basic encrustation patterns. In addition, 40% of all cells were connected to extracellular chains. This number, however, was systematically underestimated by counting cells that were not completely within the volume. Under this limitation, extracellular chains affected 33% of non-mineralized cells and 90% of shell-enclosed cells, but only 6% of cells with spiky minerals on the cell surface. For interpretation of these numbers, it has to be considered that the cells were centrifuged prior to sampling and thus aggregates containing heavily encrusted cells might be slightly overrepresented. Nevertheless, the aggregate-internal count can still provide an idea of the composition of the bacterial culture.

Further observations

The large number of blockface images that compose the FIB/SEM dataset made further observations possible. These are illustrated in Figure 2, which is a combination of views that were observed directly in the blockface images or in views of inclined planes through the reconstructed volume that were calculated using the Volume Viewer plug-in in Fiji (Barthel, 2012). We decided to show both typical views and especially unusual views to illustrate the following results. In addition to extracellular chain structures, cells could also be connected otherwise, for example, through intergrown epicellular spiky minerals (Fig. 2D) or by sharing an extracellular shell structure (Fig. 2E,F).

We observed three pairs of encrusted cells that were obviously in the process of division (Fig. 2F-H). Interestingly, they showed three different encrustation types. In none of the cases, a septum was visible. This means that the septum had either not yet formed or was not associated with iron or iron minerals. Miot *et al.* (2009b) reported an asymmetric encrustation at one of the cell poles as one important feature of BoFeN1 cells. In our datasets, we did occasionally observe accumulations of extracellular precipitates at the cell poles. In our samples, this did not appear to be a systematic feature as extracellular mineralization was generally heterogeneous. Two of the cells contained within the FIB/SEM volume showed membranous extensions at one of their cell poles (Fig. 2I,J). However, as only a very small number of cells showed these structures, and as extracellular mineralization was generally heterogeneous, it is not possible to come to any conclusions regarding the preferential presence of minerals at the poles based on the present data. Under the assumption that partly encrusted cells are still able to divide, it is possible that after division, the older cell pole would remain more heavily mineralized than the newly formed one, which was also suggested previously (Miot *et al.*, 2009b).

One advantage of 3-D analysis is the possibility to access the inside of cells. This allowed us to compare the degrees of cytoplasmic mineralization. It seemed that two fundamentally different types exist. The first type is formed by a rather

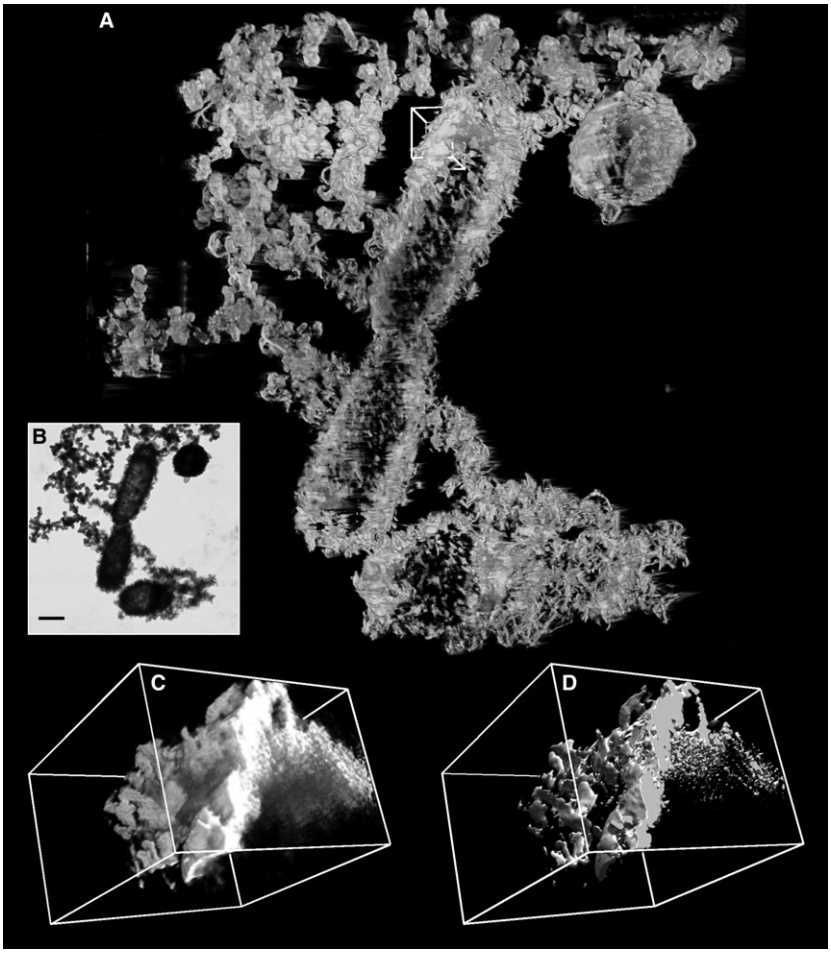

Fig. 3 3-D rendering (performed with Chimera) of the transmission electron microscopy (TEM) tomography reconstruction (A); an original projection image (0°) is provided at the lower left (B; scale bar is 500 nm). A subvolume is shown at higher magnification in 'solid' (C) and 'surface' (D) style renderings.

loosely filled cytoplasm and was usually associated with cells of the 'spiky' or 'bulky' type. This kind of mineralization appeared to start at the inside of the cell wall and to gradually extend into the cytoplasmic space (Fig. 2K). However, some mineral particles seemed to be growing inside the cytoplasm without being connected to the cell wall (Fig. 2D,I, G). The second type consisted of a very densely filled cytoplasm where only a small fraction of the cytoplasm was left free (Fig. 2E,F). This type was usually observed for cells that were enclosed by extracellular shell structures.

On a larger scale, a spatial clustering of encrustation patterns was observed for shell-enclosed cells and cells of the 'spiky' type. This is illustrated by the inclined view of the whole volume shown in Figs 2A and S3. Cells enclosed in extracellular shells as well as extracellular chains are preferably located in the upper middle part of the view, while 'spiky' cells cumulate in the lower as well as in the left regions.

Transmission electron microscopy

The TEM tomography reconstruction of samples dried onto TEM grids at an early Fe(II) oxidation stage shows some cells with a crust of spiky epicellular iron minerals (Fig. 3). In addition, some extracellular Fe-precipitates were observed. The whole cell-(iron)mineral aggregate was rather flat and appeared to be spread along the supporting Formvar membrane. The extracellular Fe-precipitates were obviously of two different types. In the upper left area, they appeared as a cloud-like, bulky structure and lack iron minerals of any defined shape, while in the lower right area, they seem to be an agglomeration of platelet-shaped iron minerals (Fig. 3A). Both types form larger agglomerations that are connected to the cells by one or several extensions. Iron minerals on the cell surfaces have a platelet-like shape, which is well shown in the detailed reconstructions (Fig. 3C,D). However, the 3-D reconstruction is affected by certain artifacts. Missing-wedge effects (Midgley & Weyland, 2003) might have caused iron minerals that were arranged perpendicular to the optical axis not to be reconstructed, and streaking artifacts create 'tails' that make the reconstructions appear elongated and bent toward the direction of the streaking (compare Fig. S4). Thus, the exact size, shape, and orientation of the iron minerals remain partly obscure, and a significant part of the iron minerals may be missing in the reconstruction. Also, other features perpendicular to the optical axis were

poorly reconstructed, which is most notably seen at the cell walls. As a consequence, certain areas of the cells remained void in the reconstructions.

Scanning transmission (soft) X-ray microscopy

In contrast to the electron microscopy-based approaches, STXM tomography provides 3-D information on the chemical composition of the sample. 3-D projections of the individual components of an air-dried cell-(iron)mineral aggregate of BoFeN1 for an early Fe(II) oxidation stage derived from the O-1s and Fe-2p edges are shown in Figs 4 and S5. The 3-D reconstructions revealed some iron mineral precipitation in the periplasm, which indicates the beginning of cell encrustation, and iron mineral precipitation in the vicinity of the cell. Gray values of the 3-D image stacks were summed up along the z-axis and could be converted into equivalent thickness (for Fe-2p and C1-s) by comparing the highest measured OD difference at the 0° measurement to the OD difference of reference spectra normalized to 1 nm (Table S1). Summarizing the gray values of all voxels within the whole 3-D component map of iron minerals (723.8–705 eV) (Figs 4A and S5A) results in a number corresponding to a total mass of 0.28 pg ferrihydrite assuming a density of 3.77 g cm^{-3} (Cornell & Schwertmann, 2004) (Table S1). The 3-D reconstruction indicates a similar encrustation pattern to the one described as cellular encrustation pattern no. 2 (Table 2). The cell can be identified in the protein component map wherein an inhomogenous distribution highlights the shape of a BoFeN1 cell (Figs 3B and S5B). In the 3-D reconstruction, almost no protein signal was found in the intracellular volume. The 3-D distribution of the biogenic Fe-precipitate derived from the O-1s edge (Figs 4C and S5C), representing a combined spectrum of a mixture of an Fe(III)-(oxyhydr)oxide phase with EPS, was very similar to the 3-D component map derived from the Fe-2p edge. Total masses calculated from the summarized gray values of the 3-D component maps obtained by O-1s fits were 0.56 pg protein, assuming a density of 1 g cm^{-3}, and 0.94 pg biogenic Fe-precipitate, using a ferrihydrite density of 3.77 g cm^{-3} (Table S1).

In contrast to the early stage of Fe(II) oxidation, 3-D component maps of a BoFeN1 cell-(iron)mineral aggregate after complete Fe(II) oxidation that were derived from the C-1s, O-1s, and Fe-2p data are shown in Figs 5 and S6. The organic carbon 3-D component map at the C-1s edge (288.2–280 eV) indicated a typical BoFeN1 cell shape with some extracellular organic carbon (representing EPS) (Figs 5A and S6A) amounting to a total mass of 0.24 pg organic carbon (mainly protein) in the whole volume, assuming a density of 1 g cm^{-3} (Table S1). The iron 3-D component map (723.8–705 eV) showed iron mineral accumulations outside the cell, within the periplasm and within the cytoplasm (Figs 5B and S6B). This could represent an encrustation pattern similar to pattern no. 6 (Table 2). The calculated total mass was 0.75 pg ferrihydrite (Table S1). The protein fit at the O-1s edge again showed a non-uniformly distributed protein signal highlighting the cell shape (Figs 5C and S6D) as well as some extracellular protein. The 3-D component map obtained by the protein fit at the O-1s edge is restricted to a slightly smaller volume compared with the organic carbon map at the C-1s edge. This could be caused by the fact that polysaccharides and lipids also more contribute to the dominant protein peak at 288.2 eV at the C-1s edge, which

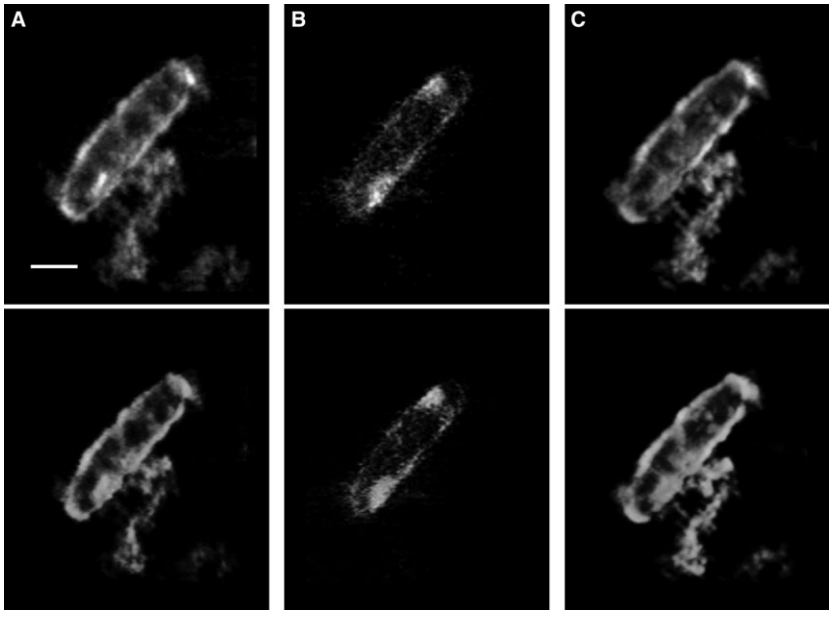

Fig. 4 Scanning transmission (soft) X-ray microscopy (STXM) 3-D reconstruction of an air-dried BoFeN1 cell at an early stage of Fe (II) oxidation (1 day). The upper row shows the maximum z-projection of the 3-D reconstructed stacks at the Fe-2p edge (A), the protein fit (B), and the biogenic Fe-precipitate fit (C) at the O-1s edge. The lower row shows the respective 3-D component maps rendered with Chimera. The different 3-D component maps (A–C) indicate a BoFeN1 cell with starting encrustation within the periplasm (scale bar 500 nm).

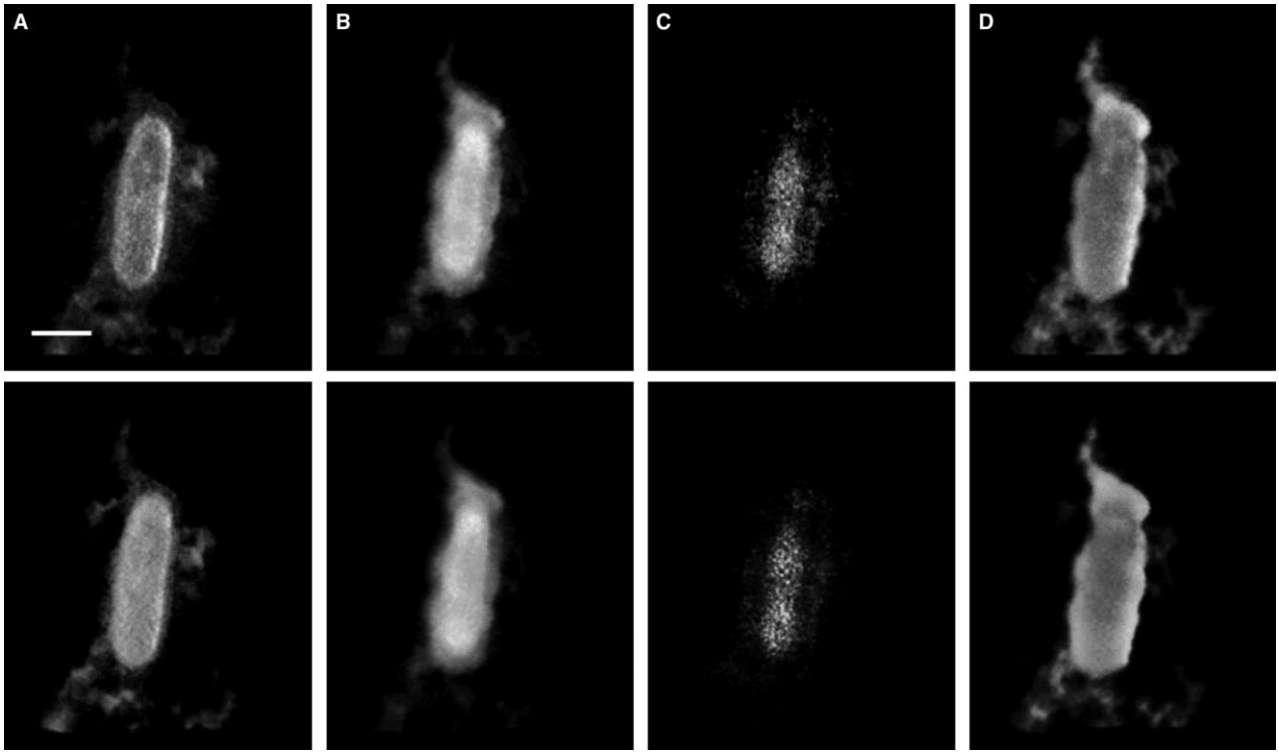

Fig. 5 Scanning transmission (soft) X-ray microscopy (STXM) 3-D reconstruction of an air-dried BoFeN1 cell after complete Fe(II) oxidation. The upper row shows the maximum z-projection of the 3-D reconstructed stacks at the C-1s edge (A), Fe-2p edge (B), the protein fit (C), and the biogenic Fe-precipitate fit (D) at the O-1s edge. The lower row shows the respective 3-D component maps rendered with Chimera. The different 3-D component maps (A–D) revealed a BoFeN1 cell after complete Fe(II) oxidation with an iron-filled cytoplasm and periplasm (scale bar 500 nm).

thus represents a mixture of different organic carbon species. The biogenic Fe-precipitate 3-D component map at the O-1s edge indicated an epicellular crust enclosing the cell (Figs 5D and S6E). This is consistently shown in the iron 3-D component map derived from the Fe-2p edge (Figs 5B and S6B). The total masses were set equivalent to the summarized gray values for whole 3-D component maps obtained by O1-s fits, and this results in 0.35 pg protein and 1.90 pg biogenic Fe-precipitate (Table S1). The calculated masses for iron (Fe2-p) and for the biogenic Fe-precipitate (O-1s) allowed to estimate a quantitative increase in the iron content from a 'weakly' periplasm-encrusted to a 'strongly' cytoplasm- and periplasm-filled BoFeN1 cell.

The BoFeN1 culture after complete Fe(II) oxidation that was prepared in a hydrated state showed a thin Fe-rich layer within the periplasm and extracellular Fe-precipitates as indicated by 3-D component maps obtained from the O-1s and Fe-2p edges in Figs 6 and S7. The iron 3-D component map (723.8–705 eV) is shown in Fig. 6A (Fig. S7A) with a calculated total mass of 0.15 pg ferrihydrite within the whole volume (Table S1). The 3-D protein map derived from the O-1s edge (Figs 6B and S7B) showed two cells, one of which was strongly associated with iron while the other one was almost iron-free, as shown by the iron 3-D component map in Figs 6A and S7A. The spatial distribution of the ferrihydrite map from the O-1s edge is similar to the 3-D component map derived from the Fe-2p edge (Figs 6C and S7D). The encrustation pattern of the BoFeN1 sample corresponds to encrustation pattern no. 2 (Table 2). In comparison with the previously presented 3-D datasets of air-dried samples, for the hydrated cells, we additionally used a spectrum of water to fit the individual components of the cell-(iron)mineral aggregate. The resulting 3-D component map of water (corrected for the homogeneous water layer of 120 nm as described in the methodology) clearly showed a hydrated cell within a cloud-like envelope that is rich in water signal as well (Figs 6D and S7D). As already shown in another study (Schmid *et al.*, 2014), high-energy-resolution measurements of BoFeN1 cells in Luxel wet cells across the entire range of the O-1s edge clearly showed the spectral signature of water around cells enclosed in the wet cell. The masses calculated from the 3-D component maps for both cells with extracellular Fe-precipitates were 0.17 pg protein, 0.60 pg ferrihydrite, and 0.29 pg water for the corrected water thickness, assuming a density of 1 g cm^{-3} for water (Table S1).

Movies of 3-D rendered datasets (S5, S6, and S7 movies) for the acquired X-ray absorption edges can be downloaded in the supporting information.

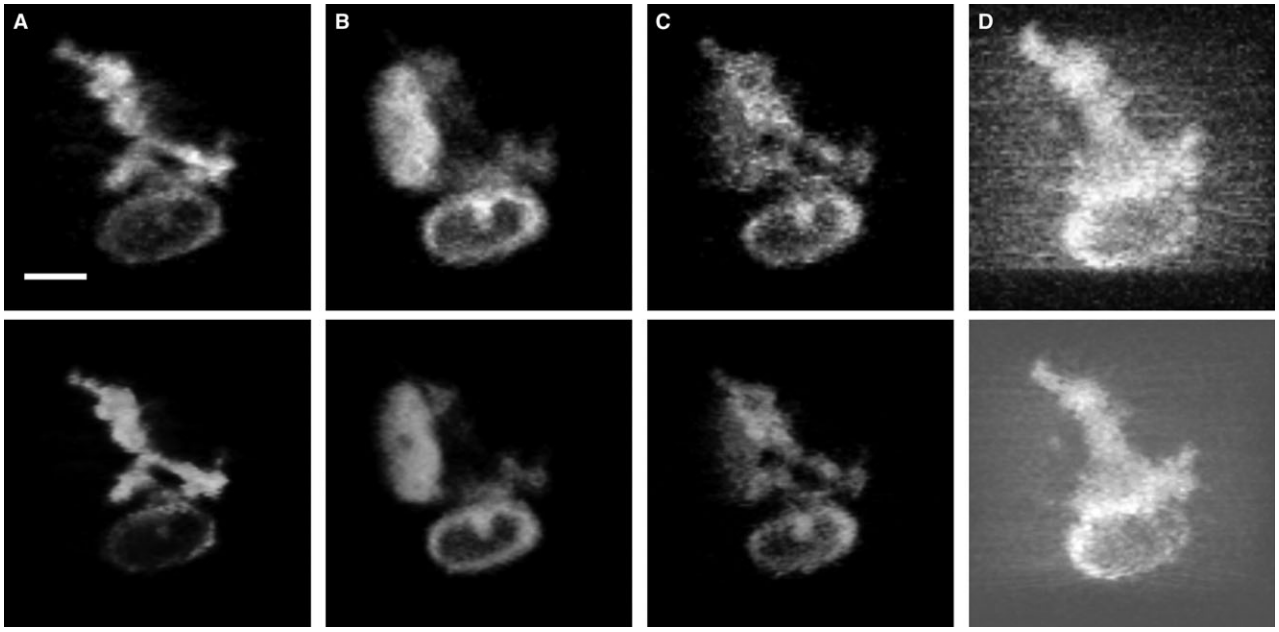

Fig. 6 Scanning transmission (soft) X-ray microscopy (STXM) 3-D reconstruction of a hydrated BoFeN1 sample after complete Fe(II) oxidation. The upper row shows the maximum z-projection of the 3-D reconstructed stacks at the Fe-2p edge (A), the protein fit (B), ferrihydrite fit (C), and water (D), corrected by addition of 120 nm at the O-1s edge. The lower row shows the respective 3-D component maps rendered with Chimera. The iron 3-D component map (A) and the ferrihydrite 3-D component map (C) indicate a BoFeN1 cell that is encrusted within the periplasm, provided by the protein 3-D component map (B). Additionally, the protein 3-D component map (B) shows a second non-encrusted cell (above the encrusted cell), which is not associated with iron (scale bar 500 nm).

Confocal laser scanning microscopy

A BoFeN1 sample after complete Fe(II) oxidation was analyzed *in vivo* with CLSM and showed aggregates of cells, iron minerals, and large quantities of EPS (Fig. 7). SYTO® 9 labels nucleic acids of Gram-negative bacteria and agglomerations of DNA to localize the cells (Fig. 7A). Sorbed but not precipitated Fe(III) is labeled by the Fe^{3+} probe (Fig. 7B), reflecting that most cells seem to be associated with sorbed Fe(III), while the degree of association with EPS and minerals varies strongly. Labeling properties of the Fe^{3+} probe are known from previous experiments with cell-(iron)mineral aggregates (Hao *et al.*, 2013). The most interesting feature is the distribution of EPS that was stained with the WGA-Alexa Fluor® 633 conjugate (Fig. 7C) that labels polysaccharides. We observed a large cloud of apparently diffuse EPS that contained numerous bacterial cells. However, cells were found outside as well as within the EPS cloud. In addition, EPS capsules enclosing the surfaces of some cells were observed. For these structures, the WGA-Alexa Fluor® 633 conjugate signal was much brighter, which indicates either higher density or stronger binding of the conjugate as compared to the EPS cloud. Iron minerals were roughly detected by their reflection of the 488-nm laser (Fig. 7D), indicating iron minerals that were intimately associated with the EPS cloud. Interestingly, the reflection signal indicated a single cell in the lower left region (Fig. 7D) that showed a strong reflection signal from either the periplasm or the cytoplasm of the cell, which would represent encrustation pattern nos. 2 or 6 (Table 2). Other encrustation patterns could not be identified due to the limited spatial resolution of CLSM.

DISCUSSION

Confirmation and extension of previous knowledge on the structure of cell-(iron)mineral aggregates

Cellular encrustation patterns described in the results section correspond well to structures that have been observed in previous studies for the nitrate-reducing *Acidovorax sp.* strain BoFeN1 during Fe(II) oxidation. Mineralization within the periplasm was reported in previous studies (Miot *et al.*, 2009b; Schaedler *et al.*, 2009), spiky minerals on the cell surface by Kappler *et al.* (2005), shells by Klueglein *et al.* (2014), and intracellular mineralization by different authors (Hitchcock *et al.*, 2012; Klueglein *et al.*, 2014). Our results consolidate prior findings and at the same time help to extend previous knowledge by providing 3-D information on the internal structure at a high spatial resolution. The structures of the precipitation patterns observed, in particular shells (no. 5) and extracellular chains of globular precipitates (no. 7) on a larger scale, can

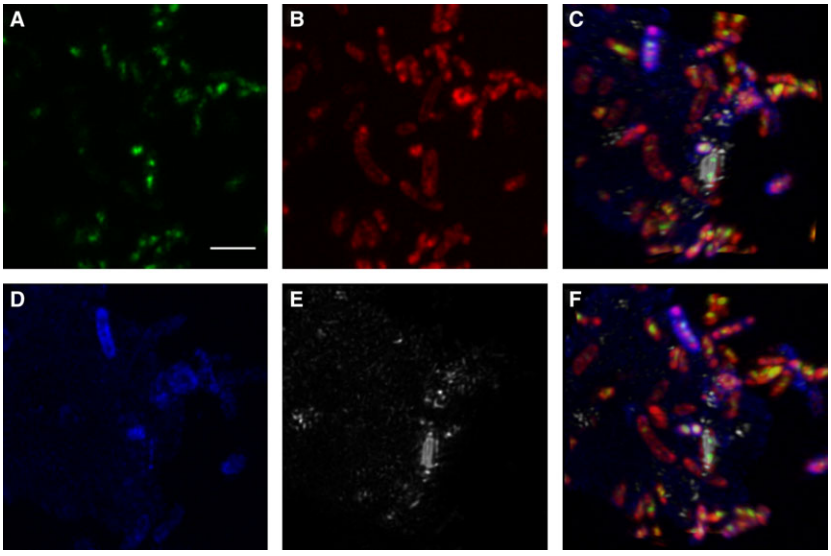

Fig. 7 Confocal laser scanning microscopy (CLSM) maximum intensity projection (A,B and D,E) images of a cell-(iron)mineral aggregate formed by BoFeN1 after complete Fe(II) oxidation. DNA labeled with SYTO® 9 (A), Fe^{3+} labeled with Fe^{3+}-probe (B), extracellular polymeric substances (EPS) labeled with Wheat Germ Agglutinin Alexa Fluor® 633 conjugate (D) and 488 nm reflection as an approximation for iron minerals (E). 3-D renderings (C,F) were carried out with Chimera and represent maximum intensity projections at different rotation angles around the *y*-axis (scale bar 2 μm).

only be unambiguously recognized from by FIB/SEM 3-D data. Miot *et al.* (2009b) also reported globules on the cell surface (on a smaller scale in a TEM tilt series), which could be explained by bulky structures on the cell surface (no. 4) or by incompletely formed shells (no. 5). Mineralized filaments as reported in the same publication probably correspond to type no. 7.

In addition to providing a complete and much more detailed picture of the structure and chemical identity of cell types, FIB/SEM tomography and CLSM allowed us to analyze larger volumes of sample. Thereby, we obtained information on the architecture of BoFeN1 cell-(iron)mineral aggregates. They appeared as network-like, interconnected structures in the FIB/SEM sample and as flocs connected loosely to an EPS cloud in CLSM, which represents the most undisturbed type of sample. The large number of cells especially within the FIB/SEM volume allowed for a systematic analysis of the abundances of the different encrustation patterns. In addition, their inhomogeneous distribution over the aggregate helped us to better understand the encrustation mechanisms. These structures were observed in a batch culture with elevated concentrations of nitrate and Fe^{2+}. In natural systems that are more complex and usually much lower in nitrate and Fe^{2+}, other processes could dominate. However, we used controlled laboratory systems to elucidate certain effects that in nature might compete with other processes. This helps also to elucidate the sorption of toxic heavy metals (e.g., As, Cu, Ni) onto cell-(iron)mineral aggregates. The sorption behavior depends on the internal structure of these cell-(iron)mineral aggregates, as shown for the inhomogenous As distribution in biogenic iron minerals formed by BoFeN1 cells (Hitchcock *et al.*, 2012).

Viability of encrusted cells

The images of cells that are completely encrusted in iron minerals raise the question whether such cells can still be viable (Klueglein *et al.*, 2014). The dividing cells shown in Figure 2F-H could indicate that even completely encrusted cells are still alive, even to the extent of being able to divide. The iron mineral encrustation of cells could serve as a protection from harmful conditions (UV light, dehydration), which is currently tested in our laboratory. One the one hand it is possible that despite the mineralization, the cells were in the process of division at the moment of fixation. On the other hand, the cells could have started to divide while still less encrusted, but have not been able to complete the division process before being immobilized by encrustation. The former scenario would have resulted not only in a non-encrusted septum, but probably also in a gradient of mineralization from the septum to the cell poles. This, however, could not be observed in any of the dividing cells. Based on our data, it cannot be proven that encrusted cells are or are not viable, but we have clearly shown that are large part of the cells are not at all affected by encrustation (28% even in a centrifuged sample). This quantity can easily account for the remaining metabolic activity of cultures that had oxidized the added Fe^{2+} to completion (Klueglein *et al.*, 2014).

EPS as an essential factor affecting cell encrustation patterns for BoFeN1

Based on our findings, we identified different encrustation patterns of BoFeN1 when cultivated with Fe^{2+} (Table 2). These were found in FIB/SEM as well as in STXM and TEM datasets. Whereas the existence of these patterns has been known before, our study provides much more extensive data. Chemically sensitive techniques, that is, STXM tomography and CLSM, indicated that iron minerals are associated with EPS, which was most reliably shown when samples could be kept wet during analysis. While we cannot derive any direct conclusions regarding the mechanism of formation of these structures, our datasets point out a dominant role of EPS in influencing their formation. Considering the different encrustation types, at least two different encrustation pathways must exist. The first would lead to a cell encrusted in epicellular spiky minerals with incomplete cytoplasmic mineralization. The second pathway would lead to cells enclosed in extracellular shells and with a much more densely filled cytoplasm. The spatial clustering of encrustation patterns observed in the FIB/SEM data suggests that the encrustation mechanism is somehow coupled to a cell's position within the cell-(iron)mineral aggregate. This could be explained by different associations of the cells with EPS. The CLSM dataset shows that some of the cells are located within an EPS cloud, whereas others are not. It is possible that cells associated with EPS develop the 'shell' type of encrustation pattern. In contrast, 'spiky' patterns (which appear to be composed of larger crystals) develop on EPS-free cells. Such cells would be found at the margins of the cell-(iron)mineral aggregates, which corresponds to the situation shown in Figure 2A. It remains unclear why a large part of the cells are not mineralized at all, despite the fact that they are placed in the direct vicinity of heavily encrusted cells.

Fe^{2+} oxidation at neutral pH results in poorly soluble Fe (III). It is likely that encrustation in Fe(III) minerals impairs diffusive exchange for the cells and that defense mechanisms against encrustation have developed. Previous studies have suggested various strategies of Fe(II)-oxidizing bacteria to prevent cell encrustation (Schaedler *et al.*, 2009). Hegler *et al.* (2010) revealed a pH decrease at the cell surface of phototrophic Fe(II)-oxidizing bacteria that can reduce the Fe(III) precipitation in vicinity to the cell by keeping it in solution and allowing it to diffuse away from the cell where it can precipitate as Fe(III) minerals, which could be associated with EPS structures. Another strategy for phototrophic Fe(II)-oxidizing bacteria is to produce organic fibers to create a redox gradient for iron oxidation in vicinity to the cells to prevent cell encrustation (Miot *et al.*, 2009c). Similar strategies were identified for the microaerophilic bacterial strains *Gallionella* and *Leptothrix*. These strains excrete organic polymers that bind Fe (III) and localize precipitation to inhibit cell encrustation. As a result, twisted stalks or sheaths are formed, which are composed of extracellular polysaccharides and Fe(III)-(oxyhydr)oxides (Chan *et al.*, 2004, 2009; Bennett *et al.*, 2014). Also, a slightly negative to neutral cell surface charge coupled with hydrophobicity could prevent cell encrustation by inhibiting the binding of positively charged Fe(III) ions (Saini & Chan, 2013). While bacterial strains that are known to be metabolic Fe(II)-oxidizers often keep their cell surfaces free of Fe(III) precipitates and sometimes form regular structures controlling Fe(III)-mineral precipitation, BoFeN1 biomineral structures appear to be less regular and also potentially harmful to the cells.

Thus, there are two main processes that influence BoFeN1 cell encrustation. Firstly, our findings show for the first time in 3-D that extracellular iron minerals and Fe(III) are closely associated with organic molecules. This is obvious in the CLSM dataset (Fig. 7) and in the 3-D component maps of organic carbon (Figs 5A and S6A) and iron (Figs 5B and S6B) of a BoFeN1 sample after complete Fe (II) oxidation that indicate that extracellular organic carbon is intimately associated with iron. Therefore, EPS production should be considered to be an essential factor affecting the cell encrustation patterns of BoFeN1. It can be excreted for several reasons, including preventing cell encrustation and lowering the toxicity of Fe^{2+}. Delayed anaerobic growth was observed for bacteria in the presence of Fe^{2+}, but toxicity of Fe^{2+} under anoxic condition remains still obscure (Poulain & Newman, 2009; Bird *et al.*, 2013). As a consequence of high Fe^{2+} concentrations, EPS can be excreted by the cells to bind dissolved Fe^{2+} ions. Previous studies revealed that EPS can bind different metals such as iron to protect the cell from encrustation (Ferris *et al.*, 1989; Mikutta *et al.*, 2012). EPS as a layer enclosing the cell and attached to the cell can lead to adsorption or complexation of Fe^{2+} and Fe^{3+} on the cell surface and in close vicinity, likely to avoid toxicity and iron mineral nucleation (Chan *et al.*, 2011). Thus, EPS can influence iron mineral formation by providing nucleation sites and therefore localizing precipitation, similar to that observed with natural bacterial populations (Clarke *et al.*, 1997; Konhauser *et al.*, 1998). In addition, Klueglein *et al.* (2014) suggested that EPS constituents could block kinks and steps of freshly precipitated iron minerals and thereby inhibit further crystal grow. This could explain the formation of 'bulky'/globular structures on the cell surface that consist of iron minerals closely associated with organic molecules (Miot *et al.*, 2009b; Schaedler *et al.*, 2009), which is also in line with our results. BoFeN1 cultivated in Fe (II)-free medium and stained with WGA-Alexa Fluor® 633 showed no fluorescence signal, indicating either the absence or a fundamentally different composition of EPS (Klueglein *et al.*, 2014). Secondly, another mechanism that could also explain cell encrustation is Fe^{2+} diffusion into

the periplasm followed by the abiotic oxidation by nitrite and/or nitric oxide as a product of denitrification (Carlson *et al.*, 2012, 2013; Klueglein *et al.*, 2014). Also, nitrite diffusion through the inner and outer cell membrane and the enclosing EPS layer could lead to extracellular Fe(II) oxidation, which—depending on the rates—might affect the mineralogy and crystal shape and thus could produce spiky, bulky, and globular structures (Klueglein *et al.*, 2014). Additionally, the formation of green rust in the form of hexagonal platelets on the cell surface as an intermediate phase could catalyze Fe(II) oxidation by nitrite with the end-product goethite (Pantke *et al.*, 2012). So far, an enzymatic pathway for Fe(II) oxidation was only indicated in a study with the *Acidovorax sp.* strain 2AN by Chakraborty & Picardal (2013). Cell encrustation could induce different potential problems to the cell as the limitation of diffusive uptake of nutrients and the discharge of metabolites. However, even from BoFeN1 culture samples taken at the stage of complete Fe(II) oxidation, it was possible to reactivate growth when spiked with fresh acetate and nitrate (Klueglein *et al.*, 2014).

In summary, it is likely that the observed encrustation patterns are a consequence of nitrite diffusion and interaction of Fe(II), Fe(III), or iron minerals with EPS. While nitrate-based Fe(II) oxidation would not be restricted to metabolically active structures such as certain enzymes, EPS could localize precipitation and/or interfere with crystal growth. STXM and CLSM results show different grades of association of cells and EPS, and different amounts or organochemical compositions that might be responsible for the development of different encrustation patterns.

Novel insights in the structure and composition of bacterial cell-(iron)mineral aggregates from the combined use of complementary tomography approaches

In this study, we subjected the nitrate-reducing *Acidovorax sp.* strain BoFeN1 to different analytical microscopy tomography methods. Each individual method provided us with insights on specific aspects of our samples. In this respect, the methods were complementary, and their combination allowed us to elucidate the native structure of BoFeN1 cell-(iron)mineral aggregates and chemical associations within these aggregates. This provides also further guidance for the interpretation of previously published data that comprise mostly 2-D surface or cross-section images. Additionally, the comparison of our results of various 3-D microscopy techniques allowed for the identification of artifacts from common sample preparation approaches such as loss or redistribution of EPS due to washing steps or dehydration/drying, respectively.

When addressing the performance of a microscopy technique, the most obvious feature is spatial resolution, defining a lower limit of the size of structures that can be resolved. Similarly, the field of view combined with the maximum sample thickness represents an upper limit. In general, confining the analysis to a smaller area of the sample will make the data less representative. Thus, in STXM and TEM tomographies, it was only possible to analyze single or a small number of cells without being able to access a large cell-(iron)mineral aggregate, which was possible in FIB/SEM and CLSM.

In addition, the mechanisms of contrast generation are of fundamental importance. TEM and FIB/SEM tomographies only yield information on electron density. To interpret such data, additional knowledge about the chemical composition of the sample is needed. CLSM offers much more diversified possibilities, as it is possible to label specific chemical species and to use a number of different fluorescent probes and corresponding channels in acquisition that each belongs to one of the species analyzed. The reliability of this information, however, is defined by the spectral properties of the fluorescent probes and by the binding selectivity of the conjugates. Unlike contrast generation by electron density or fluorescent dyes, STXM contrast is based on the intrinsic X-ray absorption properties of the sample. This allows for the determination of the chemical composition of the sample without adding labels, dyes, or stains.

Electron-dense material shown in FIB/SEM and TEM tomographies datasets was interpreted as Fe(III) minerals, as iron was the only 'heavier' element present in relevant quantities. Using STXM, in contrast, it was possible to create specific component maps to visualize the distribution of chemical species such as Fe(III) minerals and even organic molecules (referred to as organic carbon or protein). Evaluation of the spectral data can, however, introduce some error. For example, the masses obtained by fitting for the air-dried and hydrated BoFeN1 samples showed some variations between different X-ray absorption edges. Variations are found for the cumulative mass of ferrihydrite (Table S1) as evaluated by component maps obtained at the Fe-2p edge and evaluated by SVD at the O-1s edge (Table S1) for the wet-cell sample. Potential sources of error are 3-D reconstruction, background, possible absorption saturation, and variations of actual density and assumptions of density that were required for mass calculation. Higher protein content of the BoFeN1 sample at an early stage of Fe(II) oxidation could be indicative of higher cell activity (i.e., protein synthesis) compared with the sample after complete Fe(II) oxidation (Table S1), or a lack of carbon sources after extended periods of growth. The fact that the organic carbon (mainly protein signal) mass calculated at the C-1s edge is lower than the protein mass (also with some contribution of X-ray absorption by polysaccharides) calculated at the O-1s edge could be explained by higher X-ray specificity for the dominant protein peak at the C-1s edge and contributions of

polysaccharides and lipids. Despite some mass deviations between maps of the same components that were derived from different X-ray absorption edges, the major trends of 3-D chemical distributions were consistent. The cell-associated ferrihydrite mass increases, for example, from 0.28 pg for a single cell at an early Fe(II) oxidation stage to 0.75 pg after complete Fe(II) oxidation at the Fe-2p edge for air-dried STXM BoFeN1 samples. This can serve as a basis for quantitative calculations. Using the cell number of 1.1×10^9 cells mL^{-1} for BoFeN1 after 4 days (Muehe *et al.*, 2009), it is possible to calculate the theoretical amount of bound iron. With an assumed molar mass of 107 g mol^{-1} for a simplified formula of ferrihydrite ($Fe(OH)_3$), we estimate a concentration of precipitated, cell-associated iron of 0.43 mg mL^{-1} for the BoFeN1 sample after complete Fe(II) oxidation. The initial Fe^{2+} concentration of 8–10 mM corresponds to 0.45–0.56 mg mL^{-1}. This indicates that after Fe(II) oxidation, most of the iron is attached to bacterial cells. However, it has to be considered that this number is based on the analysis of a single cell, which is not necessarily representative. 2-D projections by STXM and TEM in previous studies indicated already that functional groups of the organic carbon within the periplasm (e.g., amide groups of proteins or carboxyl groups of D-glutamic acid of peptidoglycan) could be capable of trapping Fe(III)-(oxyhydr)oxide (Miot *et al.*, 2009b, 2011). Our results indicate the same trends, initial Fe(III) mineral precipitation in the periplasm with following encrustation in a 'thick' iron mineral shell/crust. Distinct from the 2-D projections, in 3-D, we could identify non-uniform distribution of organic carbon (dominated by the protein signal) for the air-dried BoFeN1 samples at an early Fe(II) oxidation stage and after complete Fe(II) oxidation, suggesting first binding of the precipitated Fe(III)-(oxyhydr)oxide/Fe(III) minerals to organic carbon in the periplasm followed by extracellular organic carbon formation associated with Fe(III)-precipitates. This result is also confirmed by nearly no X-ray absorption of extracellular organic carbon (represented by the protein signal) for the air-dried BoFeN1 cell at an early Fe(II) oxidation stage (Figs 3B and S5B). Another explanation for the missing X-ray absorption for extracellular organic carbon could be washing and drying steps during sample preparation. In contrast, a weak organic carbon signal for extracellular organic carbon is detected for the air-dried BoFeN1 cell after complete Fe(II) oxidation (Figs 5A,C and S6 A,D) and supported by the distinct protein signal for the wet-cell BoFeN1 sample (Figs 6B and S7b). In the case of the wet cell, the total number of cell-(iron)mineral aggregates that were small enough for analysis and positioned in the center of the wet cell was limited. Thus, a representative spot containing both one encrusted and one non-encrusted cell was selected for further analysis. This should be considered when comparing the amounts of Fe-minerals found in the analyzed volume, which is lower as compared to the fully encrusted cells in case of the air-dried sample.

Quantification of the protein (at the O-1s edge) and iron (at the Fe-2p edge) contents, however, has to be carried out very carefully and considering limitations. A potential source of error can be introduced during spectral fitting. In the case of the analysis of the hydrated cell, the linear fit with four components of a dataset that consisted only of three energies can affect the quality of the fit, so that additional boundary parameters (e.g., only positive values) are required. However, in our case, no pixels revealed negative values within the cell-(iron)mineral aggregate (Schmid *et al.*, 2014). Detailed comparisons of our 3-D measurements and 2-D measurements with high spectral resolution (data not shown here) indicate that the STXM tomography approach could potentially be further optimized by selecting more, and more specific, energy steps for the 3-D data acquisition. To most efficiently use the limited synchrotron beam time, often compromises in spectral resolution will be required for the relatively time-consuming angle-scan tomography measurements.

One of the major limitations of the angle-scan tomography approaches used in this study is artifact introduced during the 3-D reconstruction as discussed in more detail by different studies (Midgley & Weyland, 2003; Frank, 2006). In the present study, TEM reconstructions were considerably affected by the missing wedge (see supporting information for details). STXM tomography reconstructions are subject to the same limitations, but to a much lesser extent as a tilt range of approximately ±72° could be used for STXM instead of ±60°. In that respect, FIB/SEM tomography has the major advantage that, apart from slice alignment, no numerical reconstruction technique is applied. Thus, the brightness of a voxel results from direct acquisition by SEM imaging of the sectioned plane. In addition, datasets with almost isotropic voxels can be acquired. Likewise, in CLSM, the signals at the individual voxel positions are directly acquired and merely subjected to a deconvolution procedure following acquisition. Limitations can be caused by the absorption of the exciting laser light in thicker samples and the absorption of the emitted fluorescence light accordingly. Furthermore, because of limited numerical apertures of available lenses, the point-spread function will be elongated along the beam axis. As a result, the depth resolution is always reduced as compared to the lateral resolution.

Possible influence of preparation artifacts

In addition to limitations inherent in the analytical methods, preparation artifacts play a crucial role when dealing with biological samples. This most dramatically affects extracellular structures composed of EPS, and in our case to a much lesser extent also cell surfaces and internal

structures. In this respect, CLSM results are most reliable as CLSM permitted to analyze samples in hydrated state reflecting their natural aqueous environment (Fig. 7). In addition, no centrifugation was necessary, which could have led to distortion of delicate structures or to enrichment of cells strongly associated with iron minerals in the pellet. Although limited by moderate spatial resolution, this method gave highly valuable insights into the natural arrangement of cell-(iron)mineral aggregates especially with respect to the distribution of EPS in the natural state. When using wet cells for STXM, the calculated water content could not account for a water-immersed sample; however, the sample clearly remained hydrated despite a possible partial evaporation of the water during measurements (Fig. 6). The reconstruction showed a dense, cell-associated Fe-precipitate containing both iron minerals and proteins. As a consequence, the sample also showed a continuous distribution of extracellular organics (represented by the protein signal), which can be interpreted as EPS. In contrast to the hydrated BoFeN1 sample, the air-dried BoFeN1 sample shows an agglomeration of protein at the cell wall, which is probably due to surface tensions during air-drying (Fig. 3B, Fig. 4C) or by protein agglomeration due Fe(III) mineral precipitation. Such protein distributions were frequently reported for air-dried BoFeN1 samples (Miot *et al.*, 2009b, 2011). Some of the extracellular carbon or organic carbon associated with iron minerals of the air-dried samples can potentially also be attributed to sorption of organic carbon caused by washing the cells in deionized water, resulting in an osmotic shock, cell lysis, and release of organic carbon, as suggested in a STXM study with *Mariprofounds ferrooxydans* (Bennett *et al.*, 2014).

However, we do not expect any osmotic shock for the fully hydrated samples, and we observed larger amounts of extracellular organic carbon within those samples that were analyzed in the closest-to-natural state, that is, in CLSM and wet-cell STXM analyses. We therefore conclude that extracellular organic carbon is a part of cell-(iron)mineral aggregates in their natural state, at least when grown in the presence of Fe^{2+}. In contrast, it appears that preparation artifacts rather diminished the amount or volume of extracellular organic carbon structures in our samples. For example, longer chains of globular precipitates, such as observed in FIB/SEM tomography, could not be found in fully hydrated samples. We attribute such structures to partial collapse of EPS upon drying or dehydration, as shown by Dohnalkova *et al.* (2011). Minor distortions caused by dehydration during measurements must also be taken into account for the hydrated STXM tomography sample, but it is equally possible that no changes have occurred. Apart from the water content, dried or dehydrated structures likely retained their close-to-natural chemical composition, but considerably changed their shape upon preparation.

CONCLUSIONS

Using a variety of advanced and partly novel microscopy approaches, we acquired 3-D datasets containing both structural information and information on the chemical composition of BoFeN1 cell-(iron)mineral aggregates. These turned out to be highly heterogeneous on different spatial scales with respect to both structure and chemical composition. Our 3-D results concerning the structure of cell-(iron)mineral aggregates extend and confirm previous 2-D knowledge and provide additional guidance for the interpretation of those. Most interestingly, our chemical tomography data suggest that EPS is likely to play a key role in determining the type of mineralization pattern. While the information content of the individual datasets was sometimes limited both by the methodology and/or by sample preparation artifacts, using our complementary approach with respect to the type of information as well as to required sample preparation, a comprehensive understanding of the structure and composition of the samples was achieved.

ACKNOWLEDGMENTS

We thank C. Pantke, N. Klueglein, W. Kuerner, M. Eickhoff, E. Struve and the Geomicrobiology group Tuebingen, H. Schwarz for FIB/SEM sample preparation, T. Neu (UFZ Magdeburg) for help during screening of fluorescent dyes, Dr. J. Liu (Heliosense) for providing high-quality metal probes, T. Ayers and C. Schietinger of Luxel Corp. for development and providing tomography wet cells, A. Hitchcock for discussion. We also would like to thank the staff of the SM beamline 10ID-1 at CLS for their support. The CLS is supported by NSERC, CIHR, NRC, the Province of Saskatchewan, WEDC, and the University of Saskatchewan. 3D rendering was performed with the UCSF Chimera package developed by the RBVI at the University of California, San Francisco (supported by NIGMS P41-GM103311). This work was funded by DFG Emmy-Noether program to M.O. (OB 362/1-1).

REFERENCES

Barthel K (2012) Volume Viewer. http://rsb.info.nih.gov/ij/plugins/volume-viewer.html.

Bennett SA, Toner BM, Barco R, Edwards KJ (2014) Carbon adsorption onto Fe oxyhydroxide stalks produced by a lithotrophic iron-oxidizing bacteria. *Geobiology* **12**, 146–156.

Bird LJ, Coleman ML, Newman DK (2013) Iron and copper act synergistically to delay anaerobic growth of bacteria. *Applied and Environmental Microbiology* **79**, 3619–3627.

Biskupek J, Leschner J, Walther P, Kaiser U (2010) Optimization of STEM tomography acquisition–a comparison of convergent beam and parallel beam STEM tomography. *Ultramicroscopy* **110**, 1231–1237.

Bourdelle F, Benzerara K, Beyssac O, Cosmidis J, Neuville D, Brown G Jr, Paineau E (2013) Quantification of the ferric/

ferrous iron ratio in silicates by scanning transmission X-ray microscopy at the Fe $L_{2,3}$ edges. *Contributions to Mineralogy and Petrology* **166**, 423–434.

Carlson HK, Clark IC, Melnyk RA, Coates JD (2012) Towards a mechanistic understanding of anaerobic nitrate dependent iron oxidation: balancing electron uptake and detoxification. *Frontiers in Microbiology* **3**, 57.

Carlson HK, Clark IC, Blazewicz SJ, Iavarone AT, Coates JD (2013) Fe(II) oxidation is an innate capability of nitrate-reducing bacteria involving abiotic and biotic reactions. *Journal of Bacteriology* **195**, 3260–3268.

Chakraborty A, Picardal F (2013) Induction of nitrate-dependent Fe(II) oxidation by Fe(II) in *Dechloromonas* sp. strain UWNR4 and *Acidovorax* sp. Strain 2AN. *Applied and Environmental Microbiology* **79**, 748–752.

Chakraborty A, Roden EE, Schieber J, Picardal F (2011) Enhanced growth of *Acidovorax* sp. strain 2AN during nitrate-dependent Fe(II) oxidation in batch and continuous-flow systems. *Applied and Environmental Microbiology* **77**, 8548–8556.

Chan CS, De Stasio G, Welch SA, Girasole M, Frazer BH, Nesterova MV, Fakra S, Banfield JF (2004) Microbial polysaccharides template assembly of nanocrystal fibers. *Science* **303**, 1656–1658.

Chan CS, Fakra SC, Edwards DC, Emerson D, Banfield JF (2009) Iron oxyhydroxide mineralization on microbial extracellular polysaccharides. *Geochimica et Cosmochimica Acta* **73**, 3807–3818.

Chan CS, Fakra SC, Emerson D, Fleming EJ, Edwards KJ (2011) Lithotrophic iron-oxidizing bacteria produce organic stalks to control mineral growth: implications for biosignature formation. *ISME Journal* **5**, 717–727.

Clarke WA, Konhauser KO, Thomas JC, Bottrell SH (1997) Ferric hydroxide and ferric hydroxysulfate precipitation by bacteria in an acid mine drainage lagoon. *FEMS Microbiology Reviews* **20**, 351–361.

Cornell RM, Schwertmann U (2004) Introduction to the iron oxides. In: *The Iron Oxides*. Wiley-VCH Verlag GmbH & Co. KGaA, Weinheim, pp. 1–7.

Dohnalkova AC, Marshall MJ, Arey BW, Williams KH, Buck EC, Fredrickson JK (2011) Imaging hydrated microbial extracellular polymers: comparative analysis by electron microscopy. *Applied and Environmental Microbiology* **77**, 1254–1262.

Dynes JJ, Tyliszczak T, Araki T, Lawrence JR, Swerhone GDW, Leppard GG, Hitchcock AP (2006) Speciation and quantitative mapping of metal species in microbial biofilms using scanning transmission X-ray microscopy. *Environmental Science & Technology* **40**, 1556–1565.

Ferris FG, Schultze S, Witten TC, Fyfe WS, Beveridge TJ (1989) Metal interactions with microbial biofilms in acidic and neutral pH environments. *Applied and Environmental Microbiology* **55**, 1249–1257.

Frank J (2006) Introduction: principles of electron tomography. In *Electron Tomography* (ed Frank J). Springer New, York, pp. 1–15.

Gilbert P (1972) Iterative methods for the three-dimensional reconstruction of an object from projections. *Journal of Theoretical Biology* **36**, 105–117.

Hanhan S, Smith AM, Obst M, Hitchcock AP (2009) Optimization of analysis of soft X-ray spectromicroscopy at the Ca 2p edge. *Journal of Electron Spectroscopy and Related Phenomena* **173**, 44–49.

Hao L, Li J, Kappler A, Obst M (2013) Mapping of heavy metal ion sorption to cell-extracellular polymeric substance-mineral aggregates by using metal-selective fluorescent probes and confocal laser scanning microscopy. *Applied and Environmental Microbiology* **79**, 6524–6534.

Hegler F, Posth NR, Jiang J, Kappler A (2008) Physiology of phototrophic iron(II)-oxidizing bacteria: implications for modern and ancient environments. *FEMS Microbiology Ecology* **66**, 250–260.

Hegler F, Schmidt C, Schwarz H, Kappler A (2010) Does a low-pH microenvironment around phototrophic FeII-oxidizing bacteria prevent cell encrustation by FeIII minerals? *FEMS Microbiology Ecology* **74**, 592–600.

Henke BL, Gullikson EM, Davis JC (1993) X-Ray interactions - photoabsorption, scattering, transmission, and reflection at E=50-30,000 Ev, Z=1-92. *Atomic Data and Nuclear Data Tables* **54**, 181–342.

Hitchcock AP (2013) aXis2000 Is an IDL-Based Analytical Package. http://unicorn.mcmaster.ca/aXis2000.htmlfree, free of charge for non-commercial use.

Hitchcock AP, Johansson GA, Mitchell GE, Keefe MH, Tyliszcak T (2008) 3-d chemical imaging using angle-scan nanotomography in a soft X-ray scanning transmission X-ray microscope. *Applied Physics a-Materials Science & Processing* **92**, 447–452.

Hitchcock AP, Obst M, Wang J, Lu YS, Tyliszczak T (2012) Advances in the detection of as in environmental samples using low energy X-ray fluorescence in a scanning transmission X-ray microscope: arsenic immobilization by an Fe(II)-oxidizing freshwater bacteria. *Environmental Science & Technology* **46**, 2821–2829.

Hohmann C, Winkler E, Morin G, Kappler A (2010) Anaerobic Fe(II)-oxidizing bacteria show as resistance and immobilize as during Fe(III) mineral precipitation. *Environmental Science & Technology* **44**, 94–101.

Holzer L, Indutnyi F, Gasser PH, Münch B, Wegmann M (2004) Three-dimensional analysis of porous $BaTiO_3$ ceramics using FIB nanotomography. *Journal of Microscopy* **216**, 84–95.

Johansson GA, Tyliszczak T, Mitchell GE, Keefe MH, Hitchcock AP (2007) Three-dimensional chemical mapping by scanning transmission X-ray spectromicroscopy. *Journal of Synchrotron Radiation* **14**, 395–402.

Kappler A, Schink B, Newman DK (2005) Fe(III) mineral formation and cell encrustation by the nitrate-dependent Fe(II)-oxidizer strain BoFeN1. *Geobiology* **3**, 235–245.

Kaznatcheev KV, Karunakaran C, Lanke UD, Urquhart SG, Obst M, Hitchcock AP (2007) Soft X-ray spectromicroscopy beamline at the CLS: commissioning results. *Nuclear Instruments & Methods in Physics Research Section a-Accelerators Spectrometers Detectors and Associated Equipment* **582**, 96–99.

Klueglein N, Kappler A (2013) Abiotic oxidation of Fe(II) by reactive nitrogen species in cultures of the nitrate-reducing Fe (II) oxidizer *Acidovorax* sp. BoFeN1 - questioning the existence of enzymatic Fe(II) oxidation. *Geobiology* **11**, 180–190.

Klueglein N, Zeitvogel F, Stierhof YD, Floetenmeyer M, Konhauser KO, Kappler A, Obst M (2014) Potential role of nitrite for abiotic Fe(II) oxidation and cell encrustation during nitrate reduction by denitrifying bacteria. *Applied and Environmental Microbiology* **80**, 1051–1061.

Knott G, Rosset S, Cantoni M (2011) Focussed ion beam milling and scanning electron microscopy of brain tissue. *Journal of Visualized Experiments* **53**, e2588.

Konhauser KO (2007) *Introduction to Geomicrobiology*, Wiley-Blackwell, Malden.

Konhauser KO, Fisher QJ, Fyfe WS, Longstaffe FJ, Powell MA (1998) Authigenic mineralization and detrital clay binding by

freshwater biofilms: the Brahmani River, India. *Geomicrobiology Journal* **15**, 209–222.
Konhauser KO, Kappler A, Roden EE (2011) Iron in microbial metabolisms. *Elements* **7**, 89–93.
Koprinarov IN, Hitchcock AP, Mccrory CT, Childs RF (2002) Quantitative mapping of structured polymeric systems using singular value decomposition analysis of soft X-ray images. *Journal of Physical Chemistry B* **106**, 5358–5364.
Kremer JR, Mastronarde DN, Mcintosh JR (1996) Computer visualization of three-dimensional image data using IMOD. *Journal of Structural Biology* **116**, 71–76.
Kuehn M, Hausner M, Bungartz HJ, Wagner M, Wilderer PA, Wuertz S (1998) Automated confocal laser scanning microscopy and semiautomated image processing for analysis of biofilms. *Applied and Environmental Microbiology* **64**, 4115–4127.
Lasagni F, Lasagni A, Engstler M, Degischer HP, Mücklich F (2008) Nano-characterization of cast structures by FIB-tomography. *Advanced Engineering Materials* **10**, 62–66.
Lawrence JR, Swerhone GDW, Leppard GG, Araki T, Zhang X, West MM, Hitchcock AP (2003) Scanning transmission X-ray, laser scanning, and transmission electron microscopy mapping of the exopolymeric matrix of microbial biofilms. *Applied and Environmental Microbiology* **69**, 5543–5554.
Lawrence JR, Swerhone GD, Kuhlicke U, Neu TR (2007) In situ evidence for microdomains in the polymer matrix of bacterial microcolonies. *Canadian Journal of Microbiology* **53**, 450–458.
Mastronarde DN (1997) Dual-axis tomography: an approach with alignment methods that preserve resolution. *Journal of Structural Biology* **120**, 343–352.
Mastronarde DN (2005) Automated electron microscope tomography using robust prediction of specimen movements. *Journal of Structural Biology* **152**, 36–51.
Messaoudi C, Aschman N, Cunha M, Oikawa T, Sorzano CO, Marco S (2013) Three-dimensional chemical mapping by EFTEM-TomoJ including improvement of SNR by PCA and ART reconstruction of volume by noise suppression. *Microscopy and Microanalysis* **19**, 1669–1677.
Midgley PA, Weyland M (2003) 3D electron microscopy in the physical sciences: the development of Z-contrast and EFTEM tomography. *Ultramicroscopy* **96**, 413–431.
Mikutta R, Baumgärtner A, Schippers A, Haumaier L, Guggenberger G (2012) Extracellular polymeric substances from Bacillus subtilis associated with minerals modify the extent and rate of heavy metal sorption. *Environmental Science & Technology* **46**, 3866–3873.
Miot J, Benzerara K, Morin G, Bernard S, Beyssac O, Larquet E, Kappler A, Guyot F (2009a) Transformation of vivianite by anaerobic nitrate-reducing iron-oxidizing bacteria. *Geobiology* **7**, 373–384.
Miot J, Benzerara K, Morin G, Kappler A, Bernard S, Obst M, Ferard C, Skouri-Panet F, Guigner JM, Posth N, Galvez M, Brown GE, Guyot F (2009b) Iron biomineralization by anaerobic neutrophilic iron-oxidizing bacteria. *Geochimica et Cosmochimica Acta* **73**, 696–711.
Miot J, Benzerara K, Obst M, Kappler A, Hegler F, Schadler S, Bouchez C, Guyot F, Morin G (2009c) Extracellular iron biomineralization by photoautotrophic iron-oxidizing bacteria. *Applied and Environmental Microbiology* **75**, 5586–5591.
Miot J, Maclellan K, Benzerara K, Boisset N (2011) Preservation of protein globules and peptidoglycan in the mineralized cell wall of nitrate-reducing, iron(II)-oxidizing bacteria: a cryo-electron microscopy study. *Geobiology* **9**, 459–470.
Muehe EM, Gerhardt S, Schink B, Kappler A (2009) Ecophysiology and the energetic benefit of mixotrophic Fe(II) oxidation by various strains of nitrate-reducing bacteria. *FEMS Microbiology Ecology* **70**, 335–343.
Neu TR, Manz B, Volke F, Dynes JJ, Hitchcock AP, Lawrence JR (2010) Advanced imaging techniques for assessment of structure, composition and function in biofilm systems. *FEMS Microbiology Ecology* **72**, 1–21.
Obst M, Wang J, Hitchcock AP (2009) Soft X-ray spectro-tomography study of cyanobacterial biomineral nucleation. *Geobiology* **7**, 577–591.
Pantke C, Obst M, Benzerara K, Morin G, Ona-Nguema G, Dippon U, Kappler A (2012) Green rust formation during Fe (II) oxidation by the nitrate-reducing *Acidovorax* sp. strain BoFeN1. *Environmental Science & Technology* **46**, 1439–1446.
Pettersen EF, Goddard TD, Huang CC, Couch GS, Greenblatt DM, Meng EC, Ferrin TE (2004) UCSF Chimera—A visualization system for exploratory research and analysis. *Journal of Computational Chemistry* **25**, 1605–1612.
Poulain AJ, Newman DK (2009) Rhodobacter capsulatus catalyzes light-dependent Fe(II) oxidation under anaerobic conditions as a potential detoxification mechanism. *Applied and Environmental Microbiology* **75**, 6639–6646.
Roden EE (2012) Microbial iron-redox cycling in subsurface environments. *Biochemical Society Transactions* **40**, 1249–1256.
Saini G, Chan CS (2013) Near-neutral surface charge and hydrophilicity prevent mineral encrustation of Fe-oxidizing micro-organisms. *Geobiology* **11**, 191–200.
Schaedler S, Burkhardt C, Hegler F, Straub KL, Miot J, Benzerara K, Kappler A (2009) Formation of cell-iron-mineral aggregates by phototrophic and nitrate-reducing anaerobic Fe(II)-oxidizing bacteria. *Geomicrobiology Journal* **26**, 93–103.
Schindelin J, Arganda-Carreras I, Frise E, Kaynig V, Longair M, Pietzsch T, Preibisch S, Rueden C, Saalfeld S, Schmid B, Tinevez J-Y, White DJ, Hartenstein V, Eliceiri K, Tomancak P, Cardona A (2012) Fiji: an open-source platform for biological-image analysis. *Nature Methods* **9**, 676–682.
Schmid G, Obst M (2014) 3D chemical mapping: application of scanning transmission (soft) X-ray microscopy (STXM) in combination with angle-scan tomography in bio-, geo-, and environmental sciences. In *Electron Microscopy* (ed Kuo J). Humana Press, New York, pp. 757–781.
Schmid B, Schindelin J, Cardona A, Longair M, Heisenberg M (2010) A high-level 3D visualization API for Java and ImageJ. *BMC Bioinformatics* **11**, 274.
Schmid G, Zeitvogel F, Hao L, Ingino P, Kuerner W, Dynes JJ, Karunakaran C, Wang J, Lu Y, Ayers T, Schietinger C, Hitchcock AP, Obst M (2014) Synchrotron-based chemical nano-tomography of microbial cell-mineral aggregates in their natural, hydrated state. *Microscopy and Microanalysis* **20**, 531–536.
Sommer C, Straehle C, Kothe U, Hamprecht FA (2011) Ilastik: interactive learning and segmentation toolkit. In: *Proceedings/ IEEE International Symposium Biomedical Imaging*, IEEE, Chicago, pp. 230–233.
Sternberg SR (1983) Biomedical image processing. *Computer* **16**, 22–34.
Stewart-Ornstein J, Hitchcock AP, Cruz DH, Henklein P, Overhage J, Hilpert K, Hale JD, Hancock REW (2007) Using intrinsic X-ray absorption spectral differences to identify and map peptides and proteins. *Journal of Physical Chemistry B* **111**, 7691–7699.
Thévenaz P, Ruttimann UE, Unser M (1998) A pyramid approach to subpixel registration based on intensity. *IEEE Transactions on Image Processing* **7**, 27–41.
Vogler P (1966) Zur Analytik kondensierter Phosphate und organischer Phosphate bei limnologischen Untersuchungen.

Internationale Revue der gesamten Hydrobiologie und Hydrographie **51**, 775–785.
Wang J, Hitchcock AP, Karunakaran C, Prange A, Franz B, Harkness T, Lu Y, Obst M, Hormes J (2011) 3D chemical and elemental Imaging by STXM spectrotomography. *AIP Conference Proceedings* **1365**, 215–218.
Weber KA, Achenbach LA, Coates JD (2006) Microorganisms pumping iron: anaerobic microbial iron oxidation and reduction. *Nature Reviews Microbiology* **4**, 752–764.
Weyland M, Midgley PA (2003) Extending energy-filtered transmission electron microscopy (EFTEM) into three dimensions using electron tomography. *Microscopy and Microanalysis* **9**, 542–555.
Zhang L-F, Zhao J-L, Zeng X, Mu L, Jiang X-K, Deng M, Zhang J-X, Wei G (2011) Tuning with pH: the selectivity of a new rhodamine B derivative chemosensor for Fe3+ and Cu2+. *Sensors and Actuators B: Chemical* **160**, 662–669.

SUPPORTING INFORMATION

Additional Supporting Information may be found in the online version of this article:

Appendix S1 Descriptions of the microscopy tomography approaches.

Fig. S1 O-1s reference spectra (normalized to 1 nm) of an Fe(III)-(oxyhydr) oxide, polysaccharide, and protein (Stewart-Ornstein *et al.*, 2007) that were used to fit the datasets of air-dried BoFeN1 samples.

Fig. S2 O-1s reference spectra (normalized to 1 nm) of water, Fe(III)-(oxyhydr)oxide, and protein used for SVD for the dataset of the hydrated BoFeN1 sample.

Fig. S3 Results of focused ion beam/scanning electron microscopy (FIB/SEM) tomography: single original blockface image (A) and 3-D representation of the entire volume (performed with Chimera) (B) (scale bar 2 μm).

Fig. S4 Orthogonal views of the transmission electron microscopy (TEM) tomography reconstruction: (A) yz-plane (plane perpendicular to tilt axis; arrow indicates the direction of the optical axis); (B) xz-plane; (C) xy-plane (perpendicular to optical axis) (scale bar 500 nm).

Fig. S5 Colored 3-D component maps of the STXM dataset for the air-dried BoFeN1 cell at an early stage of Fe(II) oxidation with overlay of the different component maps.

Fig. S6 Colored 3-D component maps with overlay of the STXM dataset for a BoFeN1 cell after complete Fe(II) oxidation.

Fig. S7 Colored 3-D component maps with overlay of the STXM dataset of the wet prepared BoFeN1 sample after complete Fe(II) oxidation.

Table S1 Tabulated values (results and intermediate steps) of the quantitative calculation of the individual chemical component masses within the analyzed volumes; values from STXM tomography datasets of the air-dried BoFeN1 samples at an early stage and after complete Fe(II) oxidation, also for the hydrated BoFeN1 sample after complete Fe(II) oxidation.